**University of Alberta**

# Functional properties and organization of inspiratory neurons at the caudal and rostral boundaries of the pre-Bötzinger Complex inspiratory center in newborn rat brainstem slices

by

Nicoleta Bobocea

A thesis submitted to the Faculty of Graduate Studies and Research
in partial fulfillment of the requirements for the degree of

Master of Science

Center for Neuroscience

Edmonton, Alberta
Spring 2008

*Your file Votre référence*
*ISBN: 978-0-494-45777-1*
*Our file Notre référence*
*ISBN: 978-0-494-45777-1*

## Abstract

The pre-Bötzinger Complex (preBötC) inspiratory center remains active in a brainstem slice. Our previous study showed that the preBötC neurons can be studied with multiphoton/confocal $Ca^{2+}$ imaging in slices with identified surfaces. The present study used 500-700 μm slices with the preBötC exposed to caudal or rostral border (r+preBötC or c+preBötC slices, respectively) and 250 μm thin preBötC slices to study comparatively the structure-function relationship of caudal and rostral preBötC neurons. r+preBötC slices produced a sigh-like activity, whereas c+preBötC produced a eupnea-like activity. Multiphoton/confocal $Ca^{2+}$ imaging of neurons located caudally in the r+preBötC slices revealed a reconfiguring network, with a significantly higher number of clustered inspiratory neurons (compared to the dispersed rostral neurons in the c+preBötC slices). No rostrocaudal difference in the number of inspiratory cells was found in the thin slices suggesting that the rostrally-located structures may provide a stronger drive to preBötC inspiratory neurons than the caudally-located structures.

# Acknowledgements

I would like to thank my supervisor, Dr. Klaus Ballanyi, for his support and assistance during my graduate program and for giving me the opportunity to explore and discover new and exciting areas of neuroscience. Without his help none of my work would have been possible. To Lucia Secchia and Araya Ruangkittisakul for their patience in teaching me the experimental techniques and for their support and assistance through an always challenging and interesting experience. Their prompt and knowledgeable answers to my questions proved an invaluable addition to the development of this thesis. To my other committee members, Dr. Peter Smith and Dr. Greg Funk, for their support throughout my graduate program and highly appreciated input. I wish to thank Dr. Van Lu for her great attitude and her help during my rotation course for Neuro 501. To Darren Palathinkal for his valuable comments and for being a good colleague over the last summers. Last but not least, I wish to thank my family, my husband, Adrian, and my parents, Socrate and Valerica, for their unconditional love and support.

# Table of contents

## List of Figures

## List of abbreviations and symbols

AM, acetoxymethyl ester

pre-Bötzinger complex, preBötC

c+preBötC, slices containing caudal tissue attached to preBötC

Cadmium, $Cd^{2+}$

Calcium, $Ca^{2+}$

Calcium-activated nonspecific cation current, $I_{CAN}$

Caudal end of facial motonucleus, $VII_c$

Charge-coupled device, CCD

Cloride, $Cl^-$

Enhanced yellow fluorescent protein, EYFP

Facial motonucleus, VII

GABA, gamma amino butyric acid

Green fluorescence protein, GFP

Neurokinin-1 receptor, NK1R

Persistent $Na^+$ current, $I_{NaP}$

pFRG, parafacial respiratory group

Potassium, $K^+$

Pre-I, pre-inspiratory neurons

r+preBötC, slices containing rostral tissue attached to preBötC

Sodium, $Na^+$

Thyrotropin-releasing hormone, TRH

Ventral respiratory column, VRC

# 1. Introduction

## 1.1. Organization of mammalian respiratory centers

Breathing is a vital behaviour and it continues without cessation throughout the entire existence of most mammals. Most of the time breathing is maintained and controlled involuntarily by a neuronal network within the lower brainstem that is influenced by both peripheral and central inputs. This respiratory network is very flexible since breathing rate can also be controlled voluntarily and adjusted to various situations like physical exercise, phonation, singing, and deglutition. Such adaptability requires continuous input from higher central nervous structures such as the cortex or hypothalamus, from the peripheral chemosensitive structures of the carotid and aortic bodies, or from mechanoreceptors responsible for the lung-stretch (Hering-Breuer) reflex (McCrimmon et al., 1997; Feldman et al., 2003; Mitchell and Johnson, 2003).

Respiratory active neurons are found in three major, bilaterally organized respiratory groups. The pontine respiratory group, comprising the Kölliker-Fuse nucleus and the parabrachialis nucleus, plays an important role in generating the complex activity pattern of respiratory muscles.The dorsal respiratory group, located in the ventrolateral area of the nucleus tractus solitarius, is primarily involved in the transmission of peripheral sensory inputs to the medullary respiratory control system (Bianchi et al., 1995). The ventral respiratory column (VRC) contains aggregations of various respiratory neurons located in the ventrolateral medulla and closely associated with the nucleus ambiguus (Cohen, 1979; Richter, 1982; Long and Duffin, 1986; Bianchi et al., 1995; Duffin, 2004; Feldman and Del Negro, 2006) (Fig. 1). The integrated activity of different respiratory

groups receiving continuous modulatory inputs results in a complex pattern of respiratory activity represented by inspiratory, early-expiratory (post-inspiratory), and late-expiratory (pre-inspiratory) phases that drives respiratory muscle activities during inspiration and expiration (Richter and Spyer, 2001; Duffin, 2004).

### 1.2. In vitro isolation of respiratory centers

Analyzing the cellular mechanisms responsible for respiratory rhythm generation is difficult in intact animals because of the various interactions between neuronal groups and the diversity of modulatory afferents. Accordingly, there is a demand for reduced in vitro preparations in which the respiratory network can be studied. In the isolated neonatal rat brainstem spinal cord preparation introduced by Suzue in 1984, multiphase respiratory activity can be recorded from cranial and spinal nerves (Smith et al., 1990; Ballanyi et al., 1999). A milestone study using sectioning of the neonatal rat brainstem in vitro identified a medullary region, the pre-Bötzinger complex (preBötC), as a pivotal inspiratory center located in the ventral respiratory column (Smith et al., 1991). These sectioning experiments suggested that the preBötC extension is approximately 200 μm and it can be isolated in a transverse slice preparation that generates inspiratory rhythm.

The view that the preBötC constitutes a pivotal inspiratory center is supported since its discovery by numerous in vivo and in vitro studies (Feldman et al., 2003; Feldman and Del Negro, 2006). Local injection into the preBötC of the N-type $Ca^{2+}$ channel inhibitor ω-conotoxin GVIA or the $Na^{+}$ channel inhibitor tetrodotoxin have dramatic effects on the

centrally generated respiratory rhythm; they completely block rhythmic respiratory activity in the phrenic nerve in anesthetized adult cats (Ramirez et al., 1998). Furthermore, in anesthetized and vagotomized cats, chemical stimulation of discrete regions of the preBötC with the glutamate analogue DL-homocysteic acid produces excitatory effects on phrenic motor output (Solomon et al., 1999). In an in vitro study using neonatal rat medullary slices containing the preBötC, block of non-N-methyl-D-aspartate receptors by local application of 6-cyano-7-nitroquinoxaline-2, 3-dione into the preBötC decreased burst frequency and amplitude respectively of respiratory motor output, recorded as XII nerve rootlets activity (Funk et al., 1993). A study by Gray and collaborators (1999) demonstrated that the extent of the preBötC can be anatomically defined by a subgroup of propriobulbar respiratory neurons within the ventrolateral respiratory column expressing neurokinin-1 receptor, NK1R, a subtype of substance P receptor. Furthermore, bilateral injections of saporin conjugated substance P in the brainstem of awake adult rats, which destroyed more than 80% of preBötC NK1R neurons, resulted in an increased irregularity of breathing and alteration of blood gases and pH (Gray et al., 2001).

Despite the importance of the preBötC for breathing, it is not the only respiratory center in mammals as recently reviewed by Ballanyi and Onimaru (in preparation). Based on findings in the newborn rat en bloc preparation, it was hypothesized twenty years ago that rhythmogenic pre-/post-inspiratory active 'Pre-I' neurons provide an important synaptic drive to the inspiratory network (Onimaru et al., 1987; Onimaru and Homma, 1987). More recently, it was proposed that Pre-I neurons constitute the parafacial respiratory group, pFRG, (Onimaru and Homma, 2003). This study showed that activation of the

pFRG which innervates abdominal expiratory muscles (Janczewski et al., 2002) precedes that of the preBötC. Similar to the preBötC, the pFRG remains active, and rhythmically drives facial (VII) motoneurons, in a transverse slice of brainstem tissue that neighbours the preBötC rostrally (Onimaru et al., 2006). In addition to driving abdominal expiratory muscles, the rhythmic bursting in the pFRG slices may correspond primarily to activity in the pre-inspiratory and inspiratory phase since branches of facial nerve innervating muscles of the alae nasi were found to be active in cats and dogs during these periods in order to decrease nasal airway resistance during inspiration (Strohl, 1985; Hwang et al., 1988). Rhythmogenic interneurons in the ventrolateral aspect of the preBötC slice induce rhythmic activity of XII motoneurons, which strongly suggests that the the preBötC slice rhythm is inspiratory-related since XII motoneurons innervate the tongue during inspiration for patency of the upper airways in intact mammals (Ballanyi et al., 1999; Feldman and Del Negro, 2006).

While the slice studies showed that the preBötC and pFRG respiratory centers can principally operate independent of each other, the phase relationship between both types of rhythm and their functional interactions need to be studied in more intact models. In the newborn rat en bloc brainstem preparation and in juvenile rats in vivo these two neuronal groups seem to functionally interact. This hypothesis is primarily based on the findings that opioids do not inhibit pFRG-driven pre/postinspiratory lumbar nerve bursting in vitro, or expiratory abdominal muscle activity in vivo, but cause a quantal slowing of preBötC-driven inspiratory motor activity (Janczewski et al., 2002; Mellen et al., 2003; Janczewski and Feldman, 2006). This led to the hypothesis that the slowing of respiratory rhythm in the newborn rat en bloc medulla and in juvenile rat in vivo is, at

least partly, due to depression of synaptic excitatory transmission between the pFRG and the preBötC. It is at present discussed whether the primary site of respiratory rhythm generation in mammals is represented by the pFRG or the preBötC alone (Feldman and Janczewski, 2006a, b; Onimaru and Homma, 2006). Similarly, there is an ongoing debate on the intrinsic mechanisms of respiratory rhythm generation which will be discussed in the following section.

### 1.3. Intrinsic mechanisms of respiratory rhythm generation

The respiratory activity pattern in slices and brainstem spinal cord preparations, in which many of the afferent inputs have been eliminated, differs from that in the working-heart-brainstem preparation or in vivo models (Bianchi et al., 1995; Paton, 1996; Ballanyi et al., 1999; Richter and Spyer, 2001). In these more intact preparations, the preBötC is embedded in a neuronal network that presumably relies on $Cl^-$-mediated inhibition and also interacts on a larger scale with other structures such as the pontine respiratory group (Fung and St John, 1995, 1998; St -John and Paton, 2003; St-John and Paton, 2004). Oppositely, the transverse medullary slice represents the minimal experimental model of inspiratory activity and understanding the mechanisms that underlie inspiratory rhythm generation in the slice may serve as the basis for unraveling the mechanisms in more intact preparations.

A series of experimental data has shown that respiratory-related activity persists in vitro after pharmacologically blocking postsynaptic inhibition mediated by GABA and glycine

receptors or reducing $Cl^-$ concentration in the superfusate (Feldman and Smith, 1989; Onimaru et al., 1990; Shao and Feldman, 1997; Brockhaus and Ballanyi, 1998). This led to the hypothesis that respiratory rhythm generation is driven by neurons possessing intrinsic bursting properties (Feldman and Smith, 1989; Onimaru et al., 1989; Smith et al., 1991; Smith et al., 2000). The pacemaker properties of these neurons depend on specific ionic conductances which were identified in several studies from different groups. In a series of modeling and in vitro studies, the persistent $Na^+$ current, $I_{NaP}$, (Butera et al., 1999b, a; Del Negro et al., 2001) was found to be responsible for the intrinsic bursting properties of neonatal rodent preBötC inspiratory neurons. Their voltage-dependent bursting mechanism is unaffected by $Cd^{2+}$ but is disturbed by riluzole, which blocks $I_{NaP}$ (Del Negro et al., 2002; Ptak et al., 2005). In addition to $I_{NaP}$-dependent bursters, the preBötC contains neurons with other intrinsic conductances that promote and augment bursting. In contrast to $I_{NaP}$ pacemakers, these neurons are voltage-independent and their activity is decreased by $Cd^{2+}$ and flufenamic acid, suggesting that bursting behaviour relies on a $Ca^{2+}$-activated nonspecific cation current ($I_{CAN}$) (Pena et al., 2004; Del Negro et al., 2005). Although the respiratory rhythm stops when $I_{NaP}$ and $I_{CAN}$ are pharmacologically blocked, it can be reactivated by simply increasing neural excitability (Del Negro et al., 2005). The authors of this study concluded that $I_{NaP}$ and $I_{CAN}$ increase excitability and promote inspiratory bursts in all preBötC respiratory neurons, regardless of whether or not a reduced subset of these neurons expressing $I_{NaP}$ and $I_{CAN}$ display intrinsic bursting. Subsequently, these currents represent an important component of another theory proposed to explain the mechanism of respiratory rhythm generation, the hybrid network-pacemaker hypothesis (Feldman and Smith, 1989; Smith

et al., 1991; Richter et al., 1992). According to this hypothesis rhythmic inspiratory bursts are generated by recurrent excitatory and inhibitory synaptic connections that combine with the intrinsic membrane properties of individual neurons. Excitatory interconnections between preBötC neurons initiate positive feedback while $I_{NaP}/I_{CAN}$ conductances serve to amplify the synaptic depolarization and then generate the bursts of high-frequency spiking that characterize the typical behavior of rhythmogenic preBötC neurons. Although this hypothesis may explain various aspects involved in respiratory rhythm generation in medullary slices, further clarification of how the different elements of the preBötC network interact under standardized conditions is necessary.

### 1.4. Dependence of isolated respiratory center rhythms on dimensions of preparations and experimental conditions

Optimally, the isolated respiratory centers should be studied under in vitro conditions that closely resemble the situation in intact animals. The content of the in vitro superfusate of $K^+$ and $Ca^{2+}$, which both critically determine neuronal excitability, differs substantially between laboratories. Superfusate $K^+$ ranges from 3 mM (the physiological value) to 11 mM, whereas $Ca^{2+}$ varies between 0.8-2.4 mM (physiological range 1-1.5 mM) (Somjen, 2002; Ruangkittisakul et al., 2007). Also the physical dimensions of the in vitro models vary notably. For example, the thickness of preBötC slices varies between 200-1000 μm (Rekling et al., 1996; Koshiya and Smith, 1999). The original study indicated that the rostrocaudal extension of the preBötC is ~200 μm (Smith et al., 1991). Consequently, the rhythm generated by the inspiratory center may be modulated by neigboring structures

within the ventral respiratory column depending on both slice thickness and the relative location of the preBötC with regard to the cut slice surfaces (Ballanyi and Onimaru, 2007).

In 0-4 days-old rats, mostly used for either the en bloc preparation or preBötC slices, the rostrocaudal extension of respiratory 'marker' structures such as the inferior olive or the VII is surprisingly constant (Ruangkittisakul et al., 2006). This observation led to the generation of a reference atlas of the newborn rat medulla which can be used to produce preBötC slices with well-defined borders (Fig. 2). Such brainstem slices with the preBötC in the middle (m-preBötC slices) produced long term rhythm in physiological (3 mM) $K^+$ superfusate (Ruangkittisakul et al., 2006).

Despite the profound impact of the preBötC discovery on understanding neural respiratory control, fundamental questions remain unanswered. For example, the minimal rostrocaudal boundaries of regions sufficient and necessary for generation of fictive inspiratory rhythm in preBötC slices have not been defined yet. It is also not known whether distinct in vitro inspiratory patterns, specifically eupnea-like, sigh-like and gasp-like bursting (Lieske and Ramirez, 2006a,b; Tryba et al., 2006), depend on the rostrocaudal position of the preBötC in the slices and/or slice thickness. Generation of different inspiratory patterns may be influenced by other (respiratory) structures neighbouring the preBötC such as the rostrally located Bötzinger Complex and the pFRG which overlaps or may be identical with retrotrapezoid nucleus (Onimaru and Homma, 2003; Mulkey et al., 2004).

Using "online histology" (Ruangkittisakul et al., 2006) we have recently generated brainstem slices with variable rostrocaudal boundaries and thickness to verify the rostrocaudal boundaries of regions sufficient and necessary for generation of fictive inspiratory rhythm in preBötC slices.These slices allowed us to test our hypothesis that inspiratory-related activity patterns in 3 mM $K^+$ varies in relation to structures neighboring the preBötC. First we presented evidence that the smallest rostrocaudal preBötC extension sufficient to produce rhythm in a thin slice was 200 μm or smaller (Fig. 3A). Furthermore, only <100 μm of rhythmogenic tissue appeared to be necessary for inspiratory activity in 700 μm slices with the preBötC exposed to one surface (Fig. 4A). The latter types of slices generated fictive eupnea-like rhythm with regular burst amplitude and frequency when the isolated preBötC was neighbored by caudal tissue (Fig. 4,B). Conversely, fictive sigh-like bursts, intermingled with intersigh bursts of variable amplitude ("sigh-intersigh pattern"), were generated in slices containing the preBötC plus rostral tissue (Fig. 4,C). After spontaneous arrest of bursting, eupnea-like pattern was restored by thyrotropin-releasing hormone (TRH) or phosphodiesterase-4 inhibitors in both types of slices. In contrast, substance P or NK1R agonist reactivated sigh-intersigh pattern. This observation raised the question whether reactivation of the same pool of reconfiguring inspiratory neurons produces the two distinct inspiratory patterns (Lieske et al., 2000) or different groups of inspiratory neurons are active during a particular inspiratory pattern. It was previously shown that two-photon/confocal $Ca^{2+}$ imaging is feasible for simultaneously monitoring the activity of multiple neurons in medullary slices in order to assess whether endogenous and evoked rhythms involve the same or distinct neuronal assemblies (Ruangkittisakul et al., 2006). In the present study,

two-photon/confocal $Ca^{2+}$ imaging combined with electrophysiological recordings will be used to test the hypothesis that distinct inspiratory patterns are generated by reconfiguring network of preBötC neurons as proposed by Lieske et al. (2000).

m-preBötC slices with a thickness of 200-250 μm could generate bilaterally synchronous rhythm for time periods >1.5 h in 3 mM $K^+$ and modest elevation of superfusate $K^+$ to 6 mM restored rhythm following in vitro apnea (Fig. 3,B). The robustness and synchronicity of preBötC rhythms were further improved by the clinical respiratory stimulant theophylline (Bhatia, 2000) which acts at low millimolar concentrations likely by blocking cAMP-dependent phosphodiesterase-4 (Fredholm et al., 1999; Ruangkittisakul et al., 2006). In the 250 μm thin slices, TRH induced a eupnea-like inspiratory pattern after spontaneous arrest of rhythm (Fig. 3,C), whereas substance-P (Richter and Spyer, 2001) and NK1R agonist evoked a sigh-like pattern (Fig. 3,B,C).

### 1.5. Optical imaging of the respiratory network

Optical imaging of respiratory networks refers to visual analysis of structure-function relations in rhythmically active neuronal brainstem networks involved in control of breathing using multiphoton/confocal laser scanning microscopy or a microscope equipped with a charge-coupled device/complementary metal oxide semiconductor cameras (Ballanyi et al, in preparation). So far imaging studies of respiratory network have only been carried out in vitro, specifically in respiratory active slices, en bloc brainstem preparations from perinatal rodents and in situ arterially-perfused 'working-

heart-brainstem' preparations of both newborn and adult rodents (Koshiya and Smith, 1999, Onimaru et al., 1996, Fisher et al., 2006; Potts and Paton, 2006). Voltage-sensitive dye imaging of the activity of neuronal populations has been shown in the latter in situ models (Fisher et al., 2006; Potts and Paton, 2006). In contrast, simultaneous $Ca^{2+}$ imaging of both the activity and basic morphology of single respiratory neurons, or clusters of such cells, has so far not been reported in the perfused preparation and only in one case for en bloc medulla (Eugenin et al., 2006). In rhythmic slices, $Ca^{2+}$ imaging has primarily been done in inspiratory active interneurons and hypoglossal (XII) motoneurons (Koshyia and Smith, 1999, Ladewig and Keller, 2000, Mironov and Richter, 2001). A useful method to visualise respiratory neurons located in the VRC and more precisely in the preBötC was to fluorescently target specific receptors expressed by these neurons (Gray et al., 1999, Pagliardini et al., 2005).

### 1.5.1. Targeted recording from fluorescence-tagged respiratory neurons

It is not clear yet whether rhythmogenic respiratory neurons, specifically of the preBötC and pFRG, have specific morphological features such as a particular size and shape of the soma or number and orientation of (primary) dendrites. If this is the case, such cells could be selectively targeted after fluorescence labelling for intracellular electrophysiological recording in the rhythmic slices. Subpopulations of respiratory neurons in acute medullary slices can be labelled with fluorescent markers for proteins in the plasma membrane or cytosol. In that context, it was hypothesized that rhythmogenic preBötC neurons are characterized by postsynaptic NK1R (Gray et al., 1999). Accordingly,

fluorescence-tagging of substance P uptake via these receptors revealed that preBötC neurons can indeed be targeted (Pagliardini et al., 2005). However, it was recently found that the labelling is not specific for inspiratory preBötC neurons and included various other types of (respiratory) brainstem neurons (Hayes and Del Negro, 2007).

Currently, fluorescence-tagged transcription factors targeted to respiratory neurons are being constructed in transgenic mice. For example, in a recent report (Kuwana et al., 2006) gene targeting of enhanced green fluorescence protein (GFP) to the locus of the gene responsible for glutamic acid decarboxylase synthesis was used in combination with perforated whole cell recordings to characterize morphologically and electrophysiologically GABAergic neurons in the preBötC complex of neonatal mice. Only 20% of GFP-positive neurons in the preBötC region were inspiratory and all of the remaining GFP-positive neurons were non-respiratory. Although the morphology of GFP-positive inspiratory neurons and GFP-negative inspiratory neurons was different (GFP-positive inspiratory neurons had smaller somata size, with various shapes and 2-3 dendrites, whereas GFP-negative inspiratory neurons were multipolar and they were predominantly located around and inside the area of the nucleus ambiguous), their electrophysiological properties did not vary. Also no clear morphological or functional difference between the GFP-positive inspiratory and GFP-positive non-respiratory neurons was observed.

Another recent study (Winter et al., 2007) has shown that Thy1.2-promoter driven transgenic expression of enhanced yellow fluorescent protein in the VRC partially overlaped with respiratory neurons. Whole cell recordings targeted to preBötC neurons

labelled with EYFP revealed a population with heterogeneous electrical and morphological properties.

These two examples show that fluorescence tags promoted by transcription factors may be used for visualisation of isolated respiratory network. However, it is possible that respiratory neurons are characterized by a complex pattern of transcription factors, ionic conductances and neurotransmitter receptors, hence the need to study these neurons with multiple technical approaches.

### 1.5.2. Voltage-sensitive dye imaging of spatiotemporal respiratory patterns

Voltage-sensitive dye imaging is principally suited to measure the activity of single cells. However, in the respiratory networks this technique has been applied only to monitor, at low optical magnification, spatiotemporal activity patterns in large populations of respiratory neurons (Onimaru et al., 1996; Okada et al., 2001; Tokumasu et al., 2001). In these studies, fluorescence signals were collected from the ventral brainstem surface. Most areas of the ventral respiratory column, including the pFRG and preBötC, contain different classes of respiratory neurons and therefore their activity is not imaged with single-cell resolution in these studies in order to visualize intercellular interactions and particular patterns of activity. Despite these caveats, respiratory voltage-sensitive dye imaging provided important information regarding the organization and function of respiratory networks. In en bloc medullas from newborn rodents, voltage-sensitive dye imaging revealed that both the dorsal and pontine respiratory groups are active in regions similar to those previously identified in adult mammals with combined electrophysiological and histological techniques (Onimaru and Homma, 2005). The

important imaging study on the discovery of the pFRG showed that the area of the location of these rhythmogenic preinspiratory neurons extends further rostrally than previously assumed (Onimaru and Homma, 2003). Taken together, this shows that voltage-sensitive dye imaging is a potent tool for the analysis of spatiotemporal patterns of respiratory activities, particularly when this technique is combined with electrophysiological recording of cellular respiratory bursting.

### 1.5.3. Imaging of respiratory $Ca^{2+}$ oscillations

In excitable cells, a notable rise of the free cytosolic [$Ca^{2+}$] is associated with the $Ca^{2+}$ influx caused by activity-related depolarization. Accordingly, $Ca^{2+}$ imaging is a widely used tool for monitoring neuronal activity. In 1999, Koshiya and Smith used the $Ca^{2+}$ sensitive dye Calcium Green-1 AM to visualize the population activity of preBötC isolated in neonatal rodent brainstem (Fig. 5). non-N-methyl-D-aspartate receptors antagonist 6-cyano-7-nitroquinoxaline-2, 3-dione abolished inspiratory motor output but approximately 70 % of the labelled inspiratory neurons still generated rhythmic $Ca^{2+}$ oscillations in line with the hypothesis that preBötC neurons have pacemaker-like properties. The intrinsic bursting behaviour is preserved in even more reduced preparations, namely the preBötC "island" (Johnson et al., 2001).

A more recent study by Thoby-Brisson and collaborators (Thoby-Brisson et al., 2005) aimed to reveal the emergence of rhythmogenic circuits supporting respiratory-like activity in isolated brainstem spinal cord and medullary transverse slice preparations of

mouse embryos by means of $Ca^{2+}$ imaging coupled with electrophysiological recordings. These slices revealed two distinct types of activities: a primordial low-frequency activity characterized by initiation site in the dorsomedial medulla and dependence on gap junctions, and a high-frequency respiratory-like activity emerging at embryonic day 15 in a restricted region ventral to the nucleus ambiguus, with various characteristics of the preBötC (expression of NK1R, bilateral connections, requirement of active AMPA/kainate glutamatergic synapses, modulation by substance P and the μ-opioid receptor agonist).

pFRG and preBötC activity was measured simultaneously using $Ca^{2+}$ imaging in a novel preparation developed by Mellen's group, the tilted sagittal slab from the neonatal rat, which has the entire column of respiratory active neurons in the rostral medulla exposed at the surface (Barnes et al., 2007). This preparation allows optical assessment of neuronal activity from both preBötC and pFRG networks after labelling with the membrane permeable $Ca^{2+}$ sensitive dye Fluo-4-AM and electrophysiological recording of motor output from cervical spinal nerves C1-C4.

In a recent study of our group (Ruangkittisakul et al., 2006), inspiratory $Ca^{2+}$ oscillations were measured in preBötC slices using multiphoton/confocal microscopy. This study demonstrated that the optical activity of preBötC neurons can be monitored within 20 min after the injection of $Ca^{2+}$ dye into the preBötC (Fig. 6) as compared to "overnight" (>10 h) incubation period reported in the first $Ca^{2+}$ imaging study in preBötC-containing slices (Koshiya and Smith, 1999). As a major advantage of this approach, preBötC rhythms can be studied for several hours in physiological (3 mM) $K^+$ (Ruangkittisakul et

al., 2006). Although multiphoton microscopy was used in that report, neither the activity nor the gross morphology of preBötC neurons could be imaged at high spatial resolution at depths >80 μm into the tissue. Similar limited depth resolution was reported also in the CCD camera studies (Thoby-Brisson et al., 2005; Koshiya and Smith, 1999; Funke et al., 2007). The study of Funke and collaborators tested for means to improve tissue penetration of the $Ca^{2+}$ sensitive dye Fluo-3. Although they did not succeed to image respiratory neurons deeper than approximately 60 μm, their study showed that by combining CCD camera imaging and $Ca^{2+}$ sensitive dyes it was possible to identify several types of respiratory-active cells and analyze their activity pattern at single-cell resolution.

The previous report of our group (Ruangkittisakul et al., 2006) did not aim to study technical limitations of multiphoton/confocal microscopy such as depth resolution, the influence of temporal resolution on inspiratory $Ca^{2+}$ oscillations, and to test for means to improve visualisation of preBötC neuronal morphology. Furthermore, the report on inspiratory $Ca^{2+}$ oscillations generated by the same group of neurons during spontaneous rhythmic activity and reactivation by neuromodulator (Ruangkittisakul et al., 2006) did not aim to analyze a possible reconfiguration of inspiratory patterns which, thus, remains to be tested.

## 1.6. Objectives

Although optical imaging tools have proved to be potent in revealing respiratory related activity in rhythmic medullary slices in combination with electrophysiological recordings, further clarification on the structure-function relationship at the level of preBötC is needed. In the previous studies using preBötC-containing slices, the boundaries of such slices were not precisely identified. As a result, the recorded neurons might not always have been at the level of preBötC. Moreover, these slices were bathed in superfusates containing variable concentrations of $K^+$ and $Ca^{2+}$ which may change the membrane properties of recorded cells and their responses to neuromodulators. These varying experimental conditions may explain why results from different laboratories are not easily comparable. Online histology (Ruangkittisakul et al., 2006) can be used to produce medullary slices that have the preBötC exposed to the surface (Fig. 2) and activity of identified preBötC neurons can be visualised by means of multiphoton/confocal microscopy after labelling with $Ca^{2+}$ sensitive dye Fluo-4-AM. These calibrated slices are studied in superfusate with physiological ion concentration (3 mM $K^+$ and 1 mM $Ca^{2+}$).

With these premises, the objectives of the present study are as follows:

1.6.1. As a precondition for the $Ca^{2+}$ imaging study, the technical capabilities of multiphoton/confocal microscopy were explored to improve depth and temporal resolution and to optimize visualisation of neuronal morphology.

1.6.2. Medullary slices containing the preBötC kernel have the ability to reconfigure their activity between eupnea and sigh patterns. It is not known yet whether the same respiratory neurons or separate neuronal populations are responsible for these distinct activity patterns. To test these hypotheses, I used $Ca^{2+}$ imaging and pharmacological tools and analyzed the activity patterns in medullary slices with preBötC exposed at the caudal boundary.

1.6.3. Different structural organization of rostral and caudal aspects of the preBötC network may underlie the distinct inspiratory patterns in slices containing either rostral or caudal neighbouring tissue. This hypothesis was tested by comparing $Ca^{2+}$ oscillations and distribution of inspiratory cells in slices with preBötC exposed to the caudal or rostral border.

1.6.4. Rostral and caudal preBötC neurons in 250 μm slices with additional neighbouring tissue removed were equally driven by neuromodulators such as cAMP elevating agent theophylline. Organizational differences of respiratory neurons located on the caudal and rostral aspects of the preBötC contained in 250 μm slices were explored under this condition.

## 2. Materials and Methods

### 2.1. Preparations and Solutions

Experiments were performed on transverse brainstem slices from Sprague-Dawley (SD) and Wistar (W) rats between postnatal days (P) 0-4. All procedures were carried out in compliance with the guidelines of the Canadian Council for Animal Care and with the approval of the University of Alberta Health Sciences Laboratory Animal Services Welfare Committee. Animals were anesthetized with 2-3% isoflurane until the paw withdrawal reflex disappeared. They were then decerebrated and the neuraxis isolated at 19-22 °C in saline containing (in mM) 120 NaCl; 3 KCl; 1 $CaCl_2$; 2 $MgSO_4$; 26 $NaHCO_3$; 1.25 $NaH_2PO_4$ and 20 D-glucose (pH adjusted to 7.4 by gassing with 95% $O_2$, 5% $CO_2$). After removal of the cerebellum and transverse sectioning slightly rostral to the caudal cerebellar artery and just rostral to the $C_1$ spinal cord segment, the brainstem was glued rostral side down to a metal plate. Serial transverse sections were made with a vibratome (Leica VT1000S, Leica Microsystems, Richmond Hill, Ontario, Canada) in caudorostral direction starting at the level of the pyramid decussation and the caudal end of the inferior olive. Section thickness was reduced to 100 μm when approaching the desired level for generating a rhythmic slice as evidenced by appearance of anatomical structures that marked proximity to respiratory marker nuclei. Sections were transferred on a "hanging drop" glass slide to an upright microscope (Standard 16, magnification x32, Carl Zeiss Jena, Germany) and photographed (PL-A642-1.3 Megapixel, PixeLINK, Ottawa, Ontario, Canada) using various positions of the aperture to better visualize through the thickness of the slice. This enabled visualization of the characteristic shapes

of various subnulei of the inferior olive and immediate on-line evaluation of the rostrocaudal level of sectioning by comparison with a reference atlas of the newborn rat medulla (Ruangkittisakul et al., 2006). Useful preBötC landmarks also include the facial motonucleus rostral to the preBötC and the lateral reticular nucleus caudal to the preBötC. Rostrocaudal morphological changes of dorsal medullary nuclei, such as the XII nucleus and nucleus tractus solitarius, and the dorsal medullary extension of the 4$^{th}$ ventricle including its opening, the obex, provide additional information, in particular regarding an eventual ventral-dorsal "tilt" of the slices. When appropriate, the thickness of the last prerhythmic slice was <100 µm as this facilitated the production of a rhythmic slice with a specific boundary. For more detailed "offline" analysis of slice boundaries, pre/postrhythmic "frame" sections and rhythmic slices were fixed and stained with thionin after each experiment. Boundaries determined via surface structures in stained rhythmic 500 µm slices were very similar to targeted values. However, a 50-100 µm gap between rhythmic slices and adjacent frame sections had to be taken into account for generating preBötC slices (Ruangkittisakul et al., 2006). In rhythmic slices with a thickness <300 µm, boundaries according to the determination of surface structures were 25-50 % smaller than physical slice thickness. Determination of physical thickness of 200 µm thin sectioned agar blocks or living slices cut in superfusate indicated that the error of vibratome cutting was <8 %. Slice surface values were thus corrected by determining the mean value between slice surface and frame. Slices with the preBötC in the "middle" were labeled m-preBötC, with slice thickness and mean caudal boundary indicated in brackets. For example m-preBötC[500/-0.71] referred to 500 µm slices with mean caudal boundary at 0.71 mm caudal to the caudal end of VII ($VII_c$). In analogy with that

terminology, slices containing "rostral" or "caudal" tissue plus the preBötC were labeled "r+preBötC slices" and "c+preBötC respectively (Fig. 2,B). 250 μm thick slices contained only the preBötC with minimal amount of neighbouring tissue and had mean caudal and rostral boundaries 0.64 ± 0.03 and 0.38 ± 0.04 mm caudal to $VII_c$, respectively. r+preBötC slices had the mean caudal surface 0.61±0.03 mm caudal to $VII_c$, while the c+preBötC slices (500-700 μm thick) had the mean rostral boundary 0.42±0.04 caudal to $VII_c$. Spontaneous respiratory activity patterns of the last two types of preBötC slices recorded in superfusate with physiological $K^+$ concentration varied from uniform, short, decrementing bursts in c+preBötC slices to the pattern of intermingled small bursts and sigh-like augmented bursts characterized by incrementing rise and post-inspiratory inhibition resembling fictive sigh pattern in r+preBötC slices (Fig.4,B).

Rhythmic 250-700 μm slices were transferred to the recording chamber and fixed caudal side up (except c+preBötC slices which were positioned rostral side up) with insect pins to the silicone layer covering the bottom of the chamber (volume 1.5 ml). Superfusate was administered at 5 ml/min flow rate via a peristaltic pump (Watson-Marlow Alitea-AB, Sin-Can, Calgary, Alberta, Canada). Superfusate temperature in the recording chamber was kept at 25-27 °C (TC-324B, Harvard Apparatus, Saint-Laurent, Quebec, Canada).

## 2.2. Electrophysiological recording

Inspiratory-related preBötC neuronal population activity was recorded extracellularly with a differential amplifier (DAM 50, WPI, Sarasota, Florida, USA) via suction electrodes (outer diameter 80-250 μm) filled with superfusate, positioned on the slice surface (Fig. 7,A). For optimal recording conditions (i.e. a good signal-to-noise ratio) the electrode positioned at the preBötC level was slightly pressed into the slice or minimal suction was applied. Signals were amplified (x10k), band-pass filtered (0.3-1 kHz), integrated and recorded digitally (Powerlab/8SP, ADInstruments, Colorado Springs, Colorado, USA).

## 2.3. Agents

Agents were as follows: TRH (0.1-100 nM; stocks 1 μM and 1 mM in superfusate), rolipram (1 μM; stocks 10 mM in DMSO), theophylline (2.5 mM; powder added to superfusate), glutamate (1 mM, stock 1 M in superfusate), NK1 receptor agonist, GR 73632 (2.5 and 10 nM, stock 10mM in DMSO), Fluo-4-AM (stock 5 mM in pluronic acid, 20% in dimethyl sulfoxide further diluted to 0.5 mM in superfusate); fixation solution (4% paraformaldehyde in phosphate buffer, i.e. 1:2 mixture of 0.1 M $NaH_2PO_4$ + 0.1 M $Na_2HPO_4$ in $H_2O$, pH 7.2), staining solution (1% thionin acetate in 0.1 M sodium acetate trihydrate + 0.1 M acetic acid). Agents were obtained from Sigma-Aldrich (Canada) except salts for superfusate, sodium acetate trihydrate, acetic acid (Fisher

Scientific, Ottawa, Ontario, Canada), theophylline, glutamate (ICN Biomedicals, Costa Mesa, California, USA), Fluo-4-AM (TEF Labs Inc. Austin, Texas, USA).

### 2.4. Histological procedures

All brainstem slices, i.e. frames and rhythmic slices after experiments, were fixed over night in fixation solution (see above, Agents). Slices were incubated in phosphate buffer for 2 min and immersed in thionin solution for 45, 80, and 90-100 sec for 100-150 µm thin frame slices, 250 µm thin rhythmic slices, and 500-700 µm thick rhythmic slices, respectively. Slices were then immediately rinsed with phosphate buffer for 2 min, and consecutively "washed" with 50% ethanol (4 min) followed by phosphate buffer (2 min). Frames were transferred on a "hanging drop" glass slide to a microscope (Standard 16, magnification x32, Carl Zeiss Jena, Germany) and photographed (PL-A642-1.3 Megapixel, PixeLINK, Ottawa, Ontario, Canada). Stained rhythmic slices were photographed in phosphate buffer (PL-A686-6.6 Megapixel, PixeLINK) under a stereo microscope (Zeiss-SR15, magnification x32). Resulting pictures were compared with the reference atlas of the neonatal rat brainstem and slices borders were evaluated as distance in mm to $VII_c$.

### 2.5. Multiphoton/confocal $Ca^{2+}$ imaging

Simultaneously with extracellular preBötC neuronal population activity recording, multiphoton/confocal $Ca^{2+}$ imaging measurements were performed on the contralateral

preBötC, as recently reported (Ruangkittisakul et al., 2006). Voltage-activated $Ca^{2+}$ channels are a demonstrated feature of ventral respiratory column neurons in newborn rats (Onimaru et al., 1996, 2003, Elsen and Ramirez, 2005). Thus, imaging of cytosolic $[Ca^{2+}]$ (Yuste et al., 2006) is an appropriate tool to visualize their activity, morphological features and distribution. For this study Fluo-4-AM was used. Fluo-4-AM was derived from Fluo-3-AM, one of the most widely used fluorescent $Ca^{2+}$ indicators currently available for biological preparations. Fluo-4-AM is similar to Fluo-3 AM in several respects, including spectral properties, chemical stability, dissociation constant [$K_d$ ($Ca^{2+}$)], ease of loading, and high $Ca^{2+}$- dependent fluorescence enhancement. However, Fluo-4-AM has higher efficiency than Fluo-3-AM for absorption at 488 nm excitation wavelength and lower dye concentration can be used. Several benefits can potentially be derived from using lower dye concentrations including reducing $Ca^{2+}$ buffering effects (Fleet, 1998; Hall, 1997) and minimizing the levels of toxic by-products (formaldehyde and acetic acid) from acetoxymethyl ester hydrolysis. Alternatively, if equal concentrations of Fluo-3 and Fluo-4 are used, Fluo-4 can be excited with lower intensity illumination and yet still generate the same fluorescence signal as Fluo-3. The benefits of reduced excitation light intensity include less photobleaching of the dye and decreased cellular phototoxicity.

Membrane-permeable $Ca^{2+}$ sensitive dye Fluo-4-AM (0.5 mM in superfusate) was backfilled into a broken patch pipette (outer diameter 5-10 μm). The position of the electrode for extracellular recording was used as marker for preBötC location and an image of the injection site was taken using a low magnification objective (4x). The dye was then pressure-injected (0.7-1.0 psi) at a tissue depth of 15-20 μm for 10 min (Stosiek

et al., 2000) into the preBötC region and inspiratory activity was monitored with a suction electrode from the contralateral preBötC (Fig. 7,A). Fluorescence signals were measured using either a confocal microscope and software (20x XLUMPlanF1-NA-0.95 objective; Olympus FV300+"FluoView" software, Carsen group, Markham, Ontario, Canada) or a FV300 connected with a Ti:Saphire laser (10W Mira/Verdi, Coherent, Santa Clara, California, USA) for multiphoton $Ca^{2+}$ imaging as described previously (Ruangkittisakul et al., 2006). Within 20-30 min after the injection, labeling was sufficient to reveal basic neuronal morphology and rhythmic oscillations of fluorescence intensity that were synchronous with electrophysiologically-recorded preBötC activity. The stained areas were 200-300 μm in transversal diameter (Ruangkittisakul et al., 2006). Respiratory neurons were typically imaged at depths between 40-70 μm. Rhythmic $Ca^{2+}$ rises were visualized as increases in Fluo-4 fluorescence intensity in up to 15 cells (typically 3-8) in a single image plane (xyt measurements). The stained region was monitored using a 2-3x digital zoom and the settings for y-axis scanning were varied according to the purpose of individual type of experiments (see details in the section 2.5.2).

In order to test for optimal visualisation the morphology of cell bodies and primary dendrites "z-stack"-imaging and 3D-animation obtained with FluoView software were used. Z-stack measurements or xyz measurements are a feature of the FluoView software which allows visualization of horizontal image planes along the z-axis of the tissue performed in equal steps of predefined size (Fig. 7,B). Furthermore, the Fluoview software can be used to create animations of the summated block of frames captured during a z-stack measurement by selectively changing the angle (total angle and rotation

angle increment) of rotation on different axes. For example, a xy-plane 3D animation was generated by rotating for total angle on x-axis and y-axis of 30-45° with 1° increment (Fig. 7,C). In contrast, a lateral view (xz-plane) 3D animation was obtained by rotating x-angle for 360° with 10° increment (Fig. 7,D). The lateral view animation allows visualization of depth of staining.

### 2.5.1. Depth resolution of $Ca^{2+}$ oscilations

The majority of biological tissues strongly scatter light, making high-resolution deep imaging difficult for traditional (including confocal laser scanning) fluorescence microscopy. Using a confocal scanning microscope to image within relatively thick layer of tissue, the excitation and emission photons travel through an environment where molecular interactions will change their direction. Thus, the excitation light is spread over a much larger volume and its intensity decreased. The fluorescence emitted from a molecule within this volume can be scattered on its way to the objective so that it no longer seems to come from the scanning spot. As a result, out-of-focus light might appear to come from the scanning spot whereas in-focus light is rejected because it is scattered by more superficial layers of tissue. The resulting image has two important disadvantages: it is severely blurred and it has a very low signal-to-noise ratio. For imaging deeper tissue layers, multiphoton microscopy may be more suitable. Two-photon excitation is most widely used in biological imaging studies. Two photons that arrive simultaneously at a molecule of fluorophore need to summate their energies to produce an excited state and this summation happens only in the focal volume ($<2\ \mu m^2$). Also,

lower photon energy is equivalent to longer wavelength (near infrared) which penetrates deeper into scattering tissue providing appropriate excitation in deeper tissue layers. Emission occurs in the visible spectral range and it may still undergo significant scattering on the way to the objective. Thus, the scattering-free path determines the maximum achievable imaging depth and it depends on tissue properties such as microvasculature disposition, cellular arrangement, collagen and myelin content. The imaging depth depends also on available laser power and collection efficiency (Oheim et al., 2001). For example, 1Watt average power allows imaging depths of approximately 600-800 μm in the neocortex, in vivo (Svoboda et al., 1997; Helmchen, et al., 1999). Using multiphoton/confocal microscopy to image respiratory neurons in brainstem slices did not offer such depth resolution (Ruangkittisakul et al., 2006) possibly due to greater extent of light scattering in brain slice. The use of CCD cameras also limited visualization of neuronal structures to less than 100 μm depth (Koshiya and Smith, 1999; Barnes et al., 2007). In addition to the choice of preparations and microscopy techniques, the method of fluorescence staining may also contribute to the depth resolution obtained. The question was raised whether the limited depth resolution may be due to low dye penetration into the tissue of the pressure-injection technique. The properties that influence the tissue penetration of a fluorescent dye are as follows: molecular size and lipid solubility, tortuosity of the interstitial environment, activity of intracellular esterases, extrusion by cellular anion transport systems, and the tendency of the dye molecules to form aggregates. A recent study (Funke et al., 2007) tested different conditions for the properties enumerated above and revealed that increasing the osmolarity of the interstitial space by adding manitol during dye loading increased the

tissue depth up to which the cells were labelled. Still, cells were not imaged deeper than approximately 60 μm. Further clarification of the role of low dye penetration into deeper tissue layers or limited deep fluorescence collection in reducing the depth resolution is necessary.

### 2.5.2. Temporal resolution of inspiratory $Ca^{2+}$ oscillations

The present study used multiphoton/confocal laser scanning techniques to image $Ca^{2+}$ oscillations in respiratory neurons of preBötC. "Scanning" means that the image of each section is built up by adding information from regions that are sampled in sequence. The main drawback of scanning is that image acquisition is not as rapid as with wide-field techniques in which the entire image is acquired simultaneously. The detector is typically a photomultiplier tube which, due to fast response and low noise, is ideal for detecting weak signals (Svoboda et al, 2006). A disadvantage of this detector is a low temporal efficacy meaning that if scanning speed increases the number of photons detected per pixel may decrease dramatically and limit the quality of the acquired image. With multiphoton/confocal microscopy, scanning often takes ~1 s per frame of 512 x 512 pixel dimension. This frame rate is orders of magnitude too slow for functional optical recordings of cellular electrical events, such as neuronal action potentials, which occur on a time scale of milliseconds. Some systems attempt to increase the scanning speed of the point source by operating the fast-axis galvanometer-driven mirror at its resonance frequency (Fan et al., 1999) or by replacing it with a rotating polygon mirror (Rajadhyaksha et al., 1999). These adjustments increase the frame rate solely at the

expense of dwell time per pixel which lowers photon collection and results in degradation of the achievable signal-to-noise ratio. Other ways to increase the scanning rate without sacrificing the dwell time per pixel are by simultaneously scanning several sufficiently spaced spots, as it is done with Nipkow disk-based scanners (Petran et al., 1986) or by line scanning technique (Hernandez-Cruz et al., 1990). However, these approaches still limit the accuracy of imaging very fast processes such as action potentials in neurons or the amount of spatial information. Systems based on fast charge coupled devices allow higher scanning rates (30 Hz) but they are also confronted with side effects of increased exposure which are phototoxicity and bleaching.

For the multiphoton/confocal systems used in the present study, the influence of variable sampling rates on the resolution of inspiratory $Ca^{2+}$ oscillations was tested by selectively changing the y-axis scanning setting. Since higher sampling rates resulted in phototoxic damage of some cells, it was tested here the effect of allowing variable resting time intervals in between consecutive scans on the temporal resolution of inspiratory $Ca^{2+}$ oscillations.

### 2.5.3. Visualization of respiratory neuronal morphology

The morphology of preBötC inspiratory neurons was not resolved well in the previous studies. Voltage-sensitive dyes imaging was used so far at low optical magnification to assess electrical activity patterns in large populations of respiratory neurons in en bloc (Onimaru et al., 1996; Okada et al., 2001; Tokumasu et al., 2001; Onimaru and Homma,

2003) or in situ preparations (Fisher et al., 2006; Potts and Paton, 2006). The first $Ca^{2+}$ imaging study in rodent preBötC slices (Koshiya and Smith, 1999) did not yield high resolution images of respiratory neurons. The recent report of our group (Ruangkittisakul et al., 2006) established multiphoton/confocal $Ca^{2+}$ imaging in preBötC slices with identified boundaries but the morphology of respiratory neurons was not studied in detail. A recent study (Funke et al., 2007) reported $Ca^{2+}$ imaging of respiratory-related population activity with single-cell resolution but their method resolved cell bodies and primary dendrites in few inspiratory and expiratory neurons.

Fluo-4 fluorescence emission is weak at low cytosolic $Ca^{2+}$ (Stosiek et al., 2003; Yuste et al., 2006). Therefore cells labeled with Fluo-4-AM need to be depolarized to obtain a greater fluorescence signal for better visualization of morphological details. To assess the optimal visualization of respiratory neurons morphology, two conditions were compared: high $K^+$ superfusate and glutamate-containing solution. Also the optimal concentration for glutamate solution was studied here by comparing glutamate concentrations ranging from 100 to 500 μM.

### 2.5.4. Offline analysis of $Ca^{2+}$ imaging data

Careful observation of the online activity evolving in the selected image plane enabled in identification of different regions of interest representing cells showing rhythmic changes in fluorescence. The resulting traces were transferred from FluoView software to Microsoft Excel and were reconstructed as line plots. In order to compare the pattern of

fluorescence intensity variation with the recorded preBötC population activity both types of traces were transferred to Illustrator CS (Adobe Systems Inc., San Hose, CA, USA) and aligned according to triggers used during the experiment to indicate the start and end of each imaging measurement as well as the occurrence of inspiratory bursts. The resulting figures illustrated the relationship between $Ca^{2+}$ oscillations and inspiratory activity recorded at the level of preBötC. Furthermore, using the slices borders determined with off-line histology, the level of the optically recorded preBötC neurons was calculated in relation to the $VII_c$ (by subtracting the depth at which the active neurons were recorded from the value of the corresponding slice border). Density of inspiratory neurons in the preBötC was plotted against the cell location (as distance to $VII_c$) for each type of slice used in the project. Furthermore, the soma size of inspiratory preBötC neurons was calculated using z-stacks (encompassing approximately 10 μm above and bellow the level of the imaged cells) as area of the selected regions of interest and plotted as dot histogram versus the location of the imaged cells (as distance to $VII_c$) or averaged for the intervals representing the borders of the preBötC (between 0.6 and 0.55 mm to $VII_c$ for r+preBötC slices and between 0.45 and 0.40 mm to $VII_c$ for c+preBötC slices). In addition to number and soma size of inspiratory preBötC neurons, distribution diagrams were obtained. Overlays of slice and recording/injection sites were overlapped using the center of the slice as reference point. Regions of interest representing inspiratory cells were then superimposed on the injection site of each slice.

### 2.6. Data Analysis

Electrical preBötC activity was continuously recorded and fed into a computer at a sampling rate of 1-4 kHz. Pharmacologically reactivated rhythms were described by averaging burst rates over a 2 min time period at steady-state. Signal-to-noise ratio was calculated using mean peak amplitude of inspiratory bursts relative to a mean baseline amplitude over 4-5 respiratory cycles (signal) divided by mean baseline amplitude (noise). Values are means ± SEM except for histology (means ± SD). Significance was assessed by one-sample t-test using Sigmaplot (Systat software Inc., Point Richmond, Ca, USA).

## 3. Results

### 3.1. Technical preconditions for multiphoton/confocal $Ca^{2+}$ imaging

As discussed in the Methods section, technical capabilities of the multiphoton/confocal microscopy will be investigated in the first part of Results section in order to improve the visualization of inspiratory $Ca^{2+}$ oscillations and morphological features of the preBötC respiratory neurons.

### 3.1.1. $Ca^{2+}$ imaging depth limitation – low dye penetration or limited fluorescence emission?

The multiphoton/confocal systems used in the present study could not resolve well respiratory related $Ca^{2+}$ oscillations and respiratory cells morphology in deeper tissue layers. The question was raised whether this depth resolution limitation is due to low dye diffusion from the injection site or to scattering of emission light in the tissue. To test these two hypotheses, 200 μm thin slices were injected with Fluo-4-AM following the protocol described in Methods section and then z-stack measurements were performed at the original injection site and on the opposite side after flipping the slice. In 5 slices these measurements performed revealed a maximal depth of 60 μm for confocal system and 90 μm for two-photon system up to which labeled cells could be seen (Fig. 8,A). Images at deeper layers showed less-resolved morphological details of stained cells compared to the more superficial layers (Fig. 8,A compare cells at 50 and 70 μm). Application of glutamate (1 mM) increased the intensity of fluorescence (Fig. 8,D) but did not improve the maximal depth up to which labeled cells could be seen. Slices were flipped to measure the staining penetration from the opposite side from the injection site. Z-stack measurements revealed unspecific staining in the superficial layers (30-50 μm). Cell-specific labeling could be detected starting at 50 μm (Fig. 8,B). Subtracting 50 μm (representing the depth of labeled cells from the opposite surface to the original injecting site) from the total slice thickness of 200 μm resulted in a 150 μm tissue dye penetration at the original injection site but approximately 50 μm of the total depth could not be efficiently imaged due probably to light scattering on the emission path.

In the previous experiments, the depth at which the dye was injected was 20-30 μm (the depth of the injection electrode tip) and the resulting area of staining showed higher fluorescence intensity for more superficial layers (up to 40-50 μm depth) with gradual decrease of fluorescence intensity in deeper layers (Fig. 8,A compare cells at 50 and 70 μm). Following this observation, the Fluo-4-AM was injected in a series of 4 slices at a depth of 50-70 μm to test if a deeper injection site would improve the depth resolution and the morphological details of labeled cells in deeper tissue layers. In all 4 slices the deeper injection site did not change the maximal depth at which the fluorescence signals and morphological details of labeled neurons could be optimally resolved.

In summary, this series of experiments showed that injecting Fluo-4-AM in transverse medullary slices labeled cells up to 150 μm depth but the fluorescence signal could be collected only up to 90 μm depth using multiphoton microscopy, with progressively decreasing intensity deeper than 50 μm from the slice surface. Performing the Fluo-4-AM injection deeper in the tissue (between 50 and 70 μm) did not improve the depth resolution of $Ca^{2+}$ imaging measurements.

### 3.1.2. Temporal resolution of inspiratory $Ca^{2+}$ oscillations

Recent data showed that the preBötC-containing slices have the ability to reconfigure between a regular, eupnea-like activity with constant amplitude of bursts to a sigh-like pattern, characterized by pronounced difference between the amplitude of sighs and intersigh bursts. $Ca^{2+}$ imaging of the preBötC neuronal population that showed sigh-like

activity revealed that the increased burst amplitude recorded electrically from the preBötC was also apparent in the fluorescence signal. The scanning speed of $Ca^{2+}$ imaging measurements, an important factor determining the temporal resolution, must be fast enough to accurately capture the peak and shape of inspiratory $Ca^{2+}$ oscillations. To test this hypothesis 4 m-preBötC [550/-0.75] slices (mean caudal surface at 0.75±0.03 mm caudal to $VII_c$) were used. In all slices the inspiratory rhythm recorded electrically as neuronal population activity showed a regular, eupnea-like pattern with bursts of constant amplitude. During xyt measurements the sampling rate was determined by varying the dimensions of the y-axis. Using a 20x XLUMPlanF1-NA-0.95 objective and a 2-3x digital zoom, a full frame acquisition mode of 353x353 $\mu m^2$ was equivalent to a 1.08 s/scan rate. This sampling rate was not sufficient to accurately capture all the peaks of inspiratory $Ca^{2+}$ transients resulting in a pattern of optical activity characterized by irregular amplitude of $Ca^{2+}$ oscillations, with missing or "decapitated peaks" (Fig. 9,A). Reducing the y-axis setting to obtain a "clipped" image encompassing an area of about 353x224 $\mu m^2$ increased the scanning speed to 0.7-0.8 s/scan which was sufficient to resolve 70-100 % of the peaks of inspiratory $Ca^{2+}$ rises (Fig. 9,A). Reducing further the clip size to obtain sampling rates of 0.4-0.25 s/scan increased peak amplitude slightly. The disadvantage of such fast sampling rates is that a smaller number of rhythmic cells can be imaged simultaneously due to the reduced clip size. In addition, faster scanning rates can produce an increase in phototoxicity and photobleaching (Koester et al., 1999; Patterson and Piston, 2000). A possible solution to overcome this side effect may be to allow variable rest times in between consecutive scans. The effects of such rest times on the temporal resolution of inspiratory $Ca^{2+}$ oscillations were studied here. A clipped

image (same clip size as in Fig. 9,A) was scanned at a speed of 0.25 s/scan. Allowing the resting time of 0.25-0.5 s after each scan (resulting in total scanning speed of 0.5-0.75 s/scan) did not affect the temporal resolution of inspiratory $Ca^{2+}$ oscillations. However, some fluorescence peaks started to reduce in amplitude when the resting time was increased to 0.75 s (total scanning speed of 1 s/scan). At the total scanning speed of 1.5 s/scan, more than 50 % of the peaks could not be resolved (Fig. 9,B).

These experiments showed that a scanning rate of 0.7-0.8 s/scan can be used to provide well-resolved signals of inspiratory $Ca^{2+}$ oscillations. Higher scanning rates increased the temporal resolution at the cost of increasing phototoxicity and photobleaching. Alternatively, the faster scanning rates may be used providing that sufficient resting time (0.25-0.5 s) was allowed between consecutive scans.

### 3.1.3. Optimal conditions to study the morphology of preBötC inspiratory neurons

The morphology of preBötC inspiratory neurons was not resolved well in previous reports. A recently published paper from our group (Ruangkittisakul et al., 2006) included multiphoton/confocal images of Fluo-4-AM labeled inspiratory neurons from ventral respiratory column/preBötC (Figure 8) but the morphological details were not very clear. Hence, there is a necessity to study the optimal conditions for assessing preBötC cell morphology in rhythmic medullary slices. For this purpose two hyperpolarizing conditions were tested: high $K^+$ superfusate and glutamate-containing

solution. In all slices used for the present study increasing extracellular $K^+$ from 3 mM to 7-9 mM enhanced $Ca^{2+}$ oscillations in the inspiratory active preBötC neurons and in addition revealed prominent oscillations from proximal dendrites in most of the active cells in the imaged plane (Fig. 10,A). Next, z-stack images series were acquired in high $K^+$ superfusate and 3D reconstructions were analyzed for relevant morphological details of oscillating preBötC cells. When all the xy-planes acquired during the z-stack were summated to create the 3D image, cell bodies were well-resolved showing nuclei and clear outline of the cell bodies. However, proximal dendrites showed less fluorescence signals and distal dendrites could not be visualized. Non-oscillating cells showed brighter fluorescence signals and overlapped partly with the inspiratory preBötC neurons (Fig. 10,B).

A more powerful mean (compared to elevated $K^+$) to reveal cellular morphology is glutamate application. Glutamate-induced fluorescence signals are 3–10 times larger than those associated with spontaneous or drug induced inspiratory activity (Fig. 11,A). Fluorescence signals in the cell somata were enhanced especially in the nuclei, whereas only limited improvement was seen in the proximal dendrites. Glutamate application in short pulses (10 s) can be used during the imaging experiments to test for cellular viability or at the end of the experiment in longer application (5-10 min) to improve visualization of cellular morphological features (Fig. 10,C). In a series of 7 medullary slices 550 μm thick different concentrations of glutamate ranging from 100 μM to 500 μM were compared to evaluate the optimal concentration able to reveal close-to-maximal fluorescence intensity. Applied in short pulses of 30 s, glutamate concentrations of 100-250 μM produced non-uniform, shorter-lasting, and lower-amplitude increase of

fluorescence signals compared to the response of 500 μM (Fig. 11,B). 3D reconstructions of z-stacks recorded in glutamate offered better visualization of inspiratory neurons cell bodies and proximal dendrites compared to the morphological details revealed in high $K^+$ superfusate (Fig. 10,B,C) but the distal component of the dendritic arborization was still not accessible.

The experiments conducted in the first part of Results section were designed to test several technical limitations of multiphoton/confocal microscopy used in the present study to image inspiratory $Ca^{2+}$ oscillations in preBötC slices. Although depth resolution could not be improved, it was possible to discriminate between low dye penetration into the tissue and reduced fluorescence detection from deeper tissue layers. Also, the settings for optimal temporal resolution to allow accurate measurement of inspiratory $Ca^{2+}$ transients were assessed. Furthermore, comparing high $K^+$ superfusate and glutamate-containing solution revealed that glutamate application improves to a greater extent the visualization of preBötC neuronal somata and proximal dendrites.

### 3.2. $Ca^{2+}$ imaging of reconfiguring preBötC neurons in r+preBötC slices

As stated previously, our recent study involving electrophysiological analysis of the pattern of activity in 700 μm thick r+preBötC slices revealed that these slices produced electrical activity patterns that alternated between sigh- and eupnea-like patterns. In 3 mM $K^+$, preBötC population activity showed sigh-like pattern. After onset of in vitro apnea, TRH or rolipram evoked eupnea-like rhythm, whereas substance P and the NK1R

agonist GR73632 restored sigh-like rhythm in all slices. It was tested here whether eupnea- and sigh-like preBötC respiratory-related patterns derive from separate or rather one reconfiguring network. For this purpose $Ca^{2+}$ imaging experiments were performed in 16 r+preBötC [700/-0.61] slices (mean caudal boundary 110 μm caudal to the preBötC center). These slices were positioned with the caudal surface up to allow extracellular recording of preBötC neuronal population activity combined with contrallateral recording of rhythmic $Ca^{2+}$ transients. Within 20 min after injecting Fluo-4-AM into preBötC area, measurements were performed in a single plane at depths ranging from 40 to 70 μm below the slice surface. Up to 12 cells (typically 5-8 cells) measured in a single plane showed rhythmic oscillations that were synchronous with the inspiratory rhythm recorded from contralateral preBötC. Transitions in the amplitude and frequency of rhythmic activity recorded electrophysiologically in one preBötC area were positively correlated with $Ca^{2+}$ transients in almost all preBötC neurons imaged in the contralateral area. Specifically 88 % (TRH, n= 68) and 86 % (rolipram, n= 36) of preBötC neurons active during sigh-like rhythm changed their pattern of activity when rhythm was converted to eupnea-like pattern with these 2 agents (Fig. 12). The remaining 12 and 14 % respectively, did not show rhythmic $Ca^{2+}$ fluorescence rises in response to the drugs or subsequent application of 9 mM $K^+$, suggesting phototoxic cell damage. In 4 different slices with their surface 50 μm caudal to the preBötC center, GR73632 reactivated robust sigh-like $Ca^{2+}$ oscillations in 75 % of preBötC neurons (n= 44) that showed sigh-like oscillations prior to in vitro apnea (Fig. 13). The remaining 25 % of cells did not respond to subsequent application of 9 mM $K^+$. After washout of GR73632, rolipram induced

eupnea-like rhythm and $Ca^{2+}$ oscillations in all cells that were active during the NK1R agonist-evoked sigh-like rhythm (Fig. 13).

### 3.3. Inspiratory-related $Ca^{2+}$ oscillations study in r+preBötC versus c+preBötC slices

The previous section presented evidence that in r+preBötC slices the sigh- and eupnea-like patterns emerged from the same population of preBötC neurons capable of reconfiguring their activity. It was tested further whether neurons located at the rostral preBötC border show similar characteristics as preBötC cells that were imaged at the caudal border of the inpiratory center. For this purpose similar $Ca^{2+}$ imaging experiments were performed in 12 c+preBötC slices with a mean rostral border located 0.42±0.04 mm caudal to $VII_c$ (mean rostral boundary 120 μm rostral to the preBötC center). The first 4 experiments were performed in slices with a thickness of 700 μm and a pharmacological protocol similar to that described in section 3.2 was used. Although the same procedure for injection was followed as for r+preBötC slices, not many cells were inspiratory active on the rostral surface of the c+ preBötC slices. In the same slice, multiple injections were performed to cover a wider area but this approach failed to reveal a larger number of rhythmic cells. Following this observation, the experiments were performed in 8 more c+preBötC slices with thickness between 500 and 700 μm in which only high $K^+$ (6-9 mM) superfusate was tested in order to ensure maximal stimulation of inspiratory rhythm and $Ca^{2+}$ rises.

In the c+preBötC slices used for this study the number of inspiratory cells varied between 0 and 9 (usually 2-4) and they were primarily apparent in high $K^+$ superfusate (Fig. 14). While inspiratory neurons on the caudal side of the preBötC were organized in a continuous column with at least 5-8 active cells at each cell layer, their distribution seems to be scarce on the rostral side. The scatter plot in Fig. 15,A illustrates the difference in the total number of cells imaged on the caudal and rostral aspects of the preBötC in 7 r+preBötC (pink) and 12 c+preBötC (blue), respectively. The bar graph in Figure 15,B was obtained by comparing the average number of optically recorded inspiratory cells whose locations were at the boundaries of preBötC (0.6 to 0.55 mm to $VII_c$ in 5 r+preBötC slices, 0.45 to 0.4 mm to $VII_c$ in 5 c+preBötC). One-sample t-test showed significance with p value $<0.05$. Also, the size of inspiratory cells imaged in the r+preBötC and c+preBötC slices was calculated using FluoView software as area of the regions of interest selected during off-line analysis. Size comparison of active inspiratory cells locating at the caudal (0.60 to 0.55 mm to VIIc) and rostral (0.45 to 0.40 mm to VIIc) preBötC border, from 3 r+preBötC and 5 c+preBötC slices, respectively (Fig. 15,C), did not show a significant difference between the average size value for these two preBötC inspiratory neurons populations (Fig. 15,D). Furthermore, the inspiratory cells on the caudal side of the preBötC were apparently distributed closer together, whereas on the rostral aspect of the preBötC oscillating cells suggested a more dispersed distribution. The different density and distribution of rhythmically active cells imaged in r+preBötC and c+preBötC slices were illustrated as distribution diagrams obtained by overlaying the recording sites, injection sites, and the cell bodies location of the active inspiratory neurons for each type of slice (Fig. 16,B,C). Although both types of slice showed a

consistent location for recording sites and injection sites corresponding to the preBötC (Fig. 16,B), the number of inspiratory cells was better represented in the r+preBötC compared to the c+preBötC (Fig. 16,C).

### 3.4. $Ca^{2+}$ imaging of the caudal and rostral preBötC neurons in thin slices

The two types of slices studied above, r+preBötC and c+preBötC, showed not only two distinct activity patterns in control conditions (3 mM $K^+$) but also differences in cellular density and distribution of inspiratory cells (in 6-9 mM $K^+$). This observation may be a result of different organization of rostral and caudal preBötC neuronal populations or it can derive from different drive provided by rostral and caudal neighbouring structures. To test this hypothesis, 12 m-preBötC [250/-0.64] slices, with mean caudal and rostral border located at 0.64±0.03 mm and 0.38±0.04 mm caudal to $VII_c$, were used for $Ca^{2+}$ imaging experiments. Rhythms in these thin slices seemed to develop after longer latencies and had a rather low burst rate 6-7 mM $K^+$ (Fig. 3,B). On the other hand, cAMP-elevating phosphodiesterase blocker theophylline (2.5 mM) in 3 mM $K^+$ superfusate produced a regular, robust rhythm in all tested slices (Fig. 17,A), providing adequate conditions to assess inspiratory $Ca^{2+}$ of neurons located in the caudal and rostral aspects of the preBötC. Due to the minimal afferent input from neighbouring structures, the inspiratory neurons located on the rostral and caudal aspects of thin slices containing only the preBötC were equally driven by theophylline. This was supported by the observation that theophylline-induced increase in burst rates of inspiratory rhythms recorded on caudal versus rostral side of thin slices were not significantly different (Fig.

17,B). Although both sides of the thin slices showed similar bursting rates in response to theophylline, signal-to-noise ratio (Fig. 17,C) of extracellular populational preBötC recordings on the rostral side of the thin slices was significantly lower than that of recordings on caudal side (Fig. 17,D). Average signal-to-noise ratio of recordings sampled on the rostral side (n=6) were 42% lower than that of the caudal side (n=6).

Next, inspiratory-related $Ca^{2+}$ oscillations were assessed in the caudal and rostral aspects of preBötC under the maximal stimulation of theophylline (2.5 mM) (Fig. 18,A,B). By comparing the $Ca^{2+}$ oscillations in panel A with the corresponding electrophysiological recording, it was revealed that the inspiratory cells oscillated at a higher frequency than that of the electrophysiological recording. However, the inspiratory bursts were always synchronous with the $Ca^{2+}$ transients. The number of rhythmically active preBötC cells imaged at different depths on the caudal and rostral side of the thin slices revealed a similar distribution as shown in the scatter plot in Fig. 19,A. Correspondingly, a comparison of the average number of oscillating cells imaged at the borders of preBötC (between 0.60 and 0.55 to $VII_c$ on caudal side and between 0.45 and 0.40 mm to $VII_c$ on the rostral side of thin slices) showed no significant difference between the two extremities of the inspiratory center (Fig. 19,B). The size of inspiratory preBötC cells imaged on the caudal and rostral aspects of these thin slices was calculated as described in the previous section. The cells sampled on the caudal side were imaged in 5 thin slices (mean caudal border at 0.63±0.02 mm caudal to the $VII_c$) with cell location ranging from 0.65 to 0.55 mm caudal to $VII_c$ whereas cells imaged on the rostral side of 5 other thin slices (mean rostral border at 0.38±0.03 caudal to $VII_c$) had locations ranging from 0.45 to 0.40 mm caudal to $VII_c$ (Fig. 19,C). One-sample t-test did not show a significant

difference between the mean values of cell size located on caudal and rostral aspects of the preBötC (Fig. 19,D).Similar to the cell distribution in the r+preBötC and c+preBötC slices, the distribution diagrams suggested a condensed arrangement of rhythmically active cells in the caudal aspect of the preBötC-containing thin slices, whereas in the rostral aspect the distribution of oscillating cells was more dispersed (Fig. 20,C).

## 4. Discussion

The present work focused in the first part on investing technical limitations of the multiphoton/confocal $Ca^{2+}$ imaging in order to improve the application of this technique in preBötC slices. Secondly, multiphoton/confocal $Ca^{2+}$ imaging was used to analyse the activity and organization of inspiratory neurons located at the borders of the preBötC.

### 4.1. Methodological critique of $Ca^{2+}$ imaging in preBötC slices

Although multiphoton/confocal $Ca^{2+}$ imaging of preBötC neuronal network activity was proved to be a useful approach to assess the mechanisms involved in respiratory rhythm generation, previous studies showed that this technique had also several limitations. The first part of the present study was focussed on testing technical aspects of the multiphoton/confocal $Ca^{2+}$ imaging. Specifically, depth resolution, temporal resolution and morphological resolution of imaged neurons were analyzed and tested for potential solutions.

Depth resolution, the maximal depth at which cells can be visualized, was studied in medullary slices with a thickness of 200 μm by comparing depth profiles of Fluo-4-AM labelling at the original injecting site and on the opposite side. At the original injecting site labelled cells were imaged up to 60 μm depth for confocal system and up to 90 μm depth for multiphoton imaging. Glutamate application at the original injection site improved visualisation of cell somata in deeper layers but did not increase the depth resolution. Assessing the depth profiles on the opposite side of the flipped slices revealed labelled cells at 50 μm depth, resulting in a total staining extension of 150 μm. This result suggested that the limited depth resolution seen in the previous study (Ruangkittisakul et al., 2006) was due to the limited detection of fluorescence signal emitting from labelled cells located from ~90 to 150 μm depth. Limited fluorescence signal may be explained by light scattering in the tissue. Multiphoton microscopy offers the advantages of limited excitation to the focal volume and longer wavelength of incident light. The absence of multiphoton absorption in out-of-focus planes contrasts with confocal microscopy, where (single-photon) absorption occurs within the entire excitation light cone resulting in increased scattering and higher phototoxicity. Longer wavelength of incident light is equivalent with deeper tissue penetration. Conversely lower energy of incident photons means less phototoxicity. Still, two-photon excitation fluorescence is not immune against the effects of scattering. As an excitation beam of constant power is focused deeper into a turbid medium, the number of ballistic (unscattered) photons reaching the focus of the objective decreases exponentially with depth (Dunn et al., 2000). Additionally, the maximum achievable imaging depth depends logarithmically on available laser power. With common Ti:sapphire laser sources (1 W, 100 fs, 80 MHz), power limitations restrict

the maximum imaging depth in vivo to 350–500 μm in brain tissue depending on the labelling procedure (Denk and Svoboda, 1997; Helmchen et al., 1999; Charpak et al., 2001). Still, the difference between depth resolution reported here and that of in vivo measurements is very high. In the first study that used $Ca^{2+}$ imaging in preBötC slices (Koshiya and Smith, 1999), a depth resolution similar to that in the present study was reported (80 μm, due to optical resolution limitation), whereas the study of Thoby-Brisson and collaborators (Thoby-Brisson et al., 2005) does not specify the depth at which imaged cells were located. In one study analyzing the influence of different parameters on multiphoton microscopy depth resolution, a systematically higher transparency of the intact brain compared with acute slices was observed (Oheim et al., 2001). One parameter that could account for this difference is the different metabolic state of intact brain tissue. Brain slices have a hypoxic core and the resulting acidosis may determine protein unfolding and other molecular changes that can affect the light path through the tissue.

The temporal resolution of inspiratory $Ca^{2+}$ oscillations was assessed as it was shown to be important for an accurate detection of $Ca^{2+}$ transients. The results revealed that scanning rates of 0.7-0.8 s/scan were necessary to detect 70-100 % of the peaks. Higher scanning rates did not improve notably the temporal resolution of $Ca^{2+}$ oscillations but rather produced an increase in phototoxicity. In contrast, slower scanning rates of 1.08 s/scan used for full frame acquisition resulted in missing or incomplete peaks. Although higher sampling rates were reported in previous studies using CCD cameras (Koshiya and Smith, 1999; Thoby-Brisson et al., 2005; Barnes et al., 2007), higher temporal resolution may come at the expense of lower spatial resolution, increased phototoxicity and

increased photobleaching of the specimen due to overexposure. Although most commercial laser-scanning microscopes allow the increase of the temporal resolution by restricting the scanning to a small subregion of the image, this approach draws considerable limitations on the spatial resolution. The use of resonant galvanometers to increase the speed of scanning mirrors may bring the sampling rate in the range of video rate (30 Hz) at the expense of dwell time per pixel. Another fast-scanning method uses the acousto-optical deflector to scan the laser beam along the x-axis allowing full-frame imaging rates of 30-60 Hz (Eilers, 2000). Using confocal microscopes equipped with such technique, the spatial resolution of fluorescence images is limited to some extent because their confocal aperture is a slit, rather than a pinhole. Consequently, only a part of the out-of focus light is blocked, yielding images that are slightly blurred (Tsien and Bacskai, 1995).

For the purpose of the present study, the temporal resolution obtained by compromising with the spatial resolution of clipped images seemed to be sufficient for an accurate detection of inspiratory $Ca^{2+}$ oscillations. Photodiode-equipped microscopy system to detect single neuron $Ca^{2+}$ signals with high temporal resolution (~μs) (Morgado et al., 2007) may be used to resolve $Ca^{2+}$ transients associated with each action potential. Still, separate experiments would be required to resolve well the morphological details of studied cells.

One aim of the present study was to improve the conditions for morphological characterization of the imaged cells and for this purpose two conditions were described: high $K^+$ superfusate and glutamate-containing solution. Although increasing extracellular

$K^+$ concentration produced robust rhythms (Smith et al., 1991; Funk et al., 1993) and enhanced $Ca^{2+}$ oscillations of imaged inspiratory cells, this condition only improved moderately the visualization of cellular somata. A more potent mean to excite the active cells was bath-application of glutamate which was able to elicit an increase in fluorescence intensity 3-10 times higher than spontaneous or pharmacologically-induced activity (Ruangkittisakul et al., 2006). Combining glutamate application with z-stack measurements of active cells improved visualization of inspiratory neurons somata and to a lesser extent the appearance of proximal dendrites but failed to reveal distal processes. There are reports in the literature that showed more detailed morphologies of the respiratory neurons but mainly at the expense of functional imaging. Early studies have described respiratory neurons based on camera lucida drawings of cells that were loaded with a morphological dye such as lucifer yellow during whole-cell recordings performed in brainstem-spinal cord preparations (Onimaru and Homma, 1992; Kawai et al., 1995; Ballanyi et al., 1999). This approach allowed visualization of only one cell per recording and the morphological characterization was performed off-line. Also, camera lucida drawings were considerably difficult to perform for a large amount of recorded cells. A more recent study using transgenic labelling with fluorescent proteins (Winter et al., 2007) showed that the expression of enhanced yellow fluorescent protein overlaped only partially with respiratory active neurons. The electrophysiological recordings revealed a heterogeneous population of cells due to the fact that the fluorescent protein was expressed in both respiratory and non-respiratory neurons. This method allowed visualization of many cells simultaneously but the morphological details of imaged neurons displayed in the high magnification figures were overlapped by interstitial

fluorescence signal. Another study used gene targeting of enhanced green fluorescence protein to the locus of the GAD67 gene (isoform of glutamic acid decarboxylase) to identify GABAergic neurons in medullary transverse slices from neonatal mice (Kuwana et al., 2006). It was shown that although green fluorescent protein-positive neurons were densely distributed in the dorsolateral region of the slice and sparsely in the ventromedial region, in the preBötC region intensity of fluorescence was relatively high among areas of the ventral medulla. Only approximately 20% of labeled neurons in the preBötC area were respiratory. A clear difference between the labeled inspiratory and non-respiratory neurons was not observed regarding their electrophysiological or morphological characteristics. Comparing the inspiratory neurons that were labeled with the inspiratory neurons that did not express green fluorescent protein revealed both electrophysiological and morphological differences between these two populations of inspiratory neurons. In summary, this study showed that preBötC respiratory neurons do not possess clear distinctive morphological features to differentiate them from non-respiratory neighbouring neurons. Also, the preBötC revealed a heterogeneous population of inspiratory neurons, both electrophysiologically and morphologically.

Future work directed towards morphological characterization of preBötC respiratory neurons will need imaging methods with increased depth and spatial resolution and more specific staining procedures. Combined loading with $Ca^{2+}$-sensitive and morphological dyes (e.g. "Alexa" dyes, Lucifer Yellow, Biocytin) may enable better assessment of respiratory neuronal morphology. Also, further development of new fluorescent markers for somatic or plasma membrane proteins to label specifically preBötC respiratory neurons will prove beneficial for targeted characterization of the rhythmogenic cells.

## 4.2. Inspiratory $Ca^{2+}$ oscillations imaged in medullary slices with identified borders

In the second part of the present study, multiphoton/confocal $Ca^{2+}$ imaging coupled with extracellular preBötC population recordings was used to characterize optical activity patterns and cellular distribution in preBötC slices with defined borders and thicknesses.

### 4.2.1. $Ca^{2+}$ imaging of neurons located at caudal border of preBötC reveal a reconfiguring network

Our submitted study characterized rhythms in slices with the preBötC exposed to either the caudal border (r+preBötC) or rostral border (c+preBötC), generated with online histology, to analyze the critical rostrocaudal extension for inspiratory rhythm generation (Ruangkittisakul et al., 2007b). The original report indicated that the preBötC extends ~200 μm rostrocaudally in newborn rats (Smith et al., 1991). Most studies since then used slices ≥ 500 μm thick in elevated $K^+$ superfusate to facilitate robust motor output via XII nerve roots. It was previously shown that brainstem slices >500 μm thick are principally capable of generating inspiratory-related bursting in 3 mM $K^+$ (Smith et al., 1991, Tryba et al., 2003), and that these rhythms are stable for several hours when the preBötC is positioned in the center (Ruangkittisakul et al., 2006). Furthermore, slices >500 μm exposing the preBötC to either surface and 200-250 μm slices also generated stable rhythms in physiological superfusate (Ruangkittisakul et al., 2007b). Slices lacking tissue

rostral to the isolated preBötC generated fictive eupnea pattern, whereas a sigh-intersigh burst pattern was typically seen when only rostral tissue was attached to the preBötC kernel. These distinct inspiratory patterns in anatomically different slices of identical thickness may result from spatially-segregated (tonic) drive to the reconfiguring neurons in the preBötC kernel. Specifically, structures within (or extending into) regions caudal to the preBötC may promote drive for fictive eupnea, whereas structures located rostrally to the preBötC may drive a sigh-intersigh burst pattern. The present data do not provide evidence regarding the function or anatomical organization of these structures; it is not known yet whether these structures are non-respiratory such as the raphe (Tache et al 1995) and/or part of the ventrolateral respiratory column such as the Bötzinger Complex or the (expiratory-chemosensitive) pFRG-retrotrapezoid nucleus complex (Alheid et al., 2004; Onimaru and Homma, 2003; Mulkey et al., 2004; Feldman and Del Negro, 2006). The proposed specific drive from rostrally-neighbouring structures induces within the preBötC kernel a fictive sigh burst followed by a period of inhibition. Both these phenomena resemble the inspiratory pattern in murine preBötC slices at 8 mM $K^+$ (Lieske et al., 2000). However, in that and related studies by this group (Telgkamp et al., 2002; Lieske and Ramirez, 2006a, b), both the amplitude and frequency of bursts between fictive sighs was rather stable which led to the assumption that they represent fictive eupnea. After onset of in vitro apnea, TRH or rolipram restored fictive eupnea, whereas SP and the NK1R agonist GR73632 evoked rhythm with sigh-intersigh pattern in both slice types. Multiphoton/confocal $Ca^{2+}$-imaging revealed that the same population of neurons were capable of reconfiguring their activity between a sigh-intersigh and a fictive eupnea pattern. This supports the previous hypothesis based on

electrophysiological recording in 8 mM $K^+$ mouse slices that the preBötC is comprised of a network of reconfiguring rhythmogenic neurons (Lieske et al., 2000).

### 4.2.2. $Ca^{2+}$ imaging study of inspiratory neurons located on caudal versus rostral borders of preBötC

Multiphoton/confocal imaging of inspiratory $Ca^{2+}$ oscillations of neurons located on the caudal aspect of the preBötC in r+preBötC slices revealed that these neurons are capable to reconfigure their activity between sigh- and eupnea-like inspiratory patterns. The question was raised whether optical activity recorded from neurons located on the rostral side of preBötC in c+preBötC slices would reveal a similar reconfiguring network. Surprisingly, the rostral aspect of the preBötC showed a lower number of active Fluo-4-AM loaded cells with a dispersed distribution compared to the compact arrangement of oscillating cells imaged on the caudal side of preBötC. It was more difficult to locate active inspiratory neurons in the c+preBötC slices and in such cases multiple dye-injections were applied but with limited success. Consequently, comparison between the caudal and rostral aspects of the preBötC inspiratory network was studied in 6-9 mM $K^+$ superfusate for notable stimulation of inspiratory rhythm and $Ca^{2+}$ rises. Although such conditions elicited robust inspiratory rhythm in the c+preBötC slices, the number of inspiratory neurons imaged in these slices was still significantly lower than in the r+preBötC slices. A recent study from Mellen's group (Barnes et al., 2007) also reported a non-uniform distribution of respiratory active neurons along the rostrocaudal axis of the brainstem although the point of maximal cellular density at the level of preBötC does not

coincide with the present study. The active cells showed a bimodal distribution with a peak at the caudal end of the VII motonucleus (the present study did not aim to sample cells in that area) and the other peak approximately 350 μm caudal to the first pool. The caudal group had a position on the rostrocaudal axis that corresponds to 0.35 mm caudal to $VII_c$ in our notation which is 50 μm rostral from the rostral end of preBötC, the site of low inspiratory cells density reported here. The difference may be explained by the use of different preparations in these two studies. The neonatal rat tilted sagittal slab preparation used in Mellen's group study retains brainstem structures located more rostrally (Bötzinger complex, RTN/pFRG) whose interaction with the preBötC resulted in a very complex organization of respiratory neuronal network. An alternative explanation for the lower number of inspiratory cells imaged on the rostral aspect of preBötC in our study may reflect a lack of proper dye uptake by some of these rostral preBötC inspiratory neurons, possibly due to i) the low activity of cytoplasmic esterases that do not efficiently hydrolyze the AM form of the dye and hence do not retain it inside the cell or ii) the presence of membrane transporters that may control dye extrusion from the cells. This hypothesis was contradicted by the fact that glutamate application elicited intense fluorescence from a large number of neurons located on the rostral aspect of the preBötC.

The present study also compared the size of neuronal somata of inspiratory cells located on the caudal and rostral borders of preBötC and found no significant difference between these two neuronal groups. Previous reports which analyzed preBötC neurons morphologies (Kuwana et al., 2006; Winter et al., 2007, Onimaru et al., 2003) revealed a similarly heterogeneous population of respiratory neurons at the level of preBötC.

At present, it is not known whether preBötC neurons located in the rostral aspect of the inspiratory center are capable of reconfiguring their activity. Thus, further analysis of their inspiratory $Ca^{2+}$ oscillations during bath-application of pharmacological agents that elicit sighs (substance P, NK1R agonist) or eupnea-like activity (TRH, rolipram) is necessary to answer this question.

### 4.2.3. Inspiratory $Ca^{2+}$ oscillations imaged on the caudal versus rostral aspects of thin preBötC slices

The preBötC neighboured by either rostral or caudal tissue produces two different activity patterns: sigh-like and eupnea-like. In thin slices, lacking surrounding tissue, the activity of the inspiratory neurons located on the caudal and rostral sides of the preBötC was equally driven by theophylline, a cAMP phosphodiesterase inhibitor shown to effectively stimulate robust inspiratory rhythm in medullary slices (Ruangkittisakul et al., 2006; Ruangkittisakul et al., 2007b). The number of inspiratory cells imaged on the caudal and rostral aspects of preBötC-containing thin slices was not significantly different although the distribution diagram showed different arrangements for the two opposite sides: the caudal side showed a grouped localization of active cells whereas oscillating cells imaged on rostral side were more dispersed. Lower signal-to-noise ratio revealed by electrophysiological recordings on the rostral side compared to the caudal side may also be a consequence of a dispersed distribution of inspiratory cells on the rostral side of the preBötC. A better signal-to-noise ratio suggests a better signal which may be generated by a closer distribution of recorded neurons. The fact that there was no

significant difference in the number of inspiratory neurons imaged on the caudal side of these thin slices compared to the rostral side argues against the hypothesis that inspiratory neurons located at the rostral border of the preBötC retain less dye than those situated at the caudal border. The similar number of inspiratory cells imaged on the caudal and rostral aspects of thin preBötC-containing slices as opposed to the significantly larger number of rhythmically oscillating neurons recorded in r+preBötC slices compared to c+preBötC slices may be well explained by the different drive received by preBötC inspiratory neurons in these types of slices. In the thin slices, in the absence of neighbouring structures the preBötC neurons were equally driven by theophylline whereas in the r+preBötC and c+preBötC slices the preBötC neurons were neighboured by either rostral or caudal structures respectively. As shown by the different activity pattern of these two types of slices recorded in 3 mM $K^+$ superfusate, these neighbouring structures may provide distinct drive to the preBötC kernel resulting also in a different number of inspiratory cells.

In addition to comparison of number and localization of inspiratory cells on the caudal and rostral aspects of thin preBötC-containing slices, the size of neuronal somata was also comparatively analyzed. Similar to the r+preBötC and c+preBötC slices, the soma size varied considerably on both sides of thin slices yielding average values that did not show a significant difference.

## 5. Conclusion and Perspectives

The present study showed that multiphoton/confocal $Ca^{2+}$ imaging, although presenting technical limitations, provides a potent tool for a structure-function analysis of identified preBötC neurons, in particular when combined with electrophysiological recordings. Further advancement may result with use of morphological fluorescent dyes. Neurons in the caudal aspect of preBötC are capable of reconfiguring their activity between sigh- and eupnea-like inspiratory patterns, whereas it is not known yet whether preBötC neurons located on the rostral aspect possess similar functional properties. Rhythmically active cells imaged in r+preBötC versus c+preBötC slices appeare to show a higher density on the caudal aspect of preBötC. In contrast, comparing the caudal and rostral sides of thin preBötC slices yielded a similar number of inspiratory neurons active on both sides, suggesting that differential drives from additional caudal and rostral structures may determine the number of active cells. The soma size of preBötC inspiratory neurons, as revealed by the present study, was not homogeneous but it also did not seem to differ systematically between caudal and rostral preBötC neuronal population. The neuronal structures rostrally neighbouring the preBötC may provide a stronger drive for inspiratory neurons than the caudal brainstem structures as suggested by the larger number of oscillating cells present in r+preBötC slices.

# 6. Figures

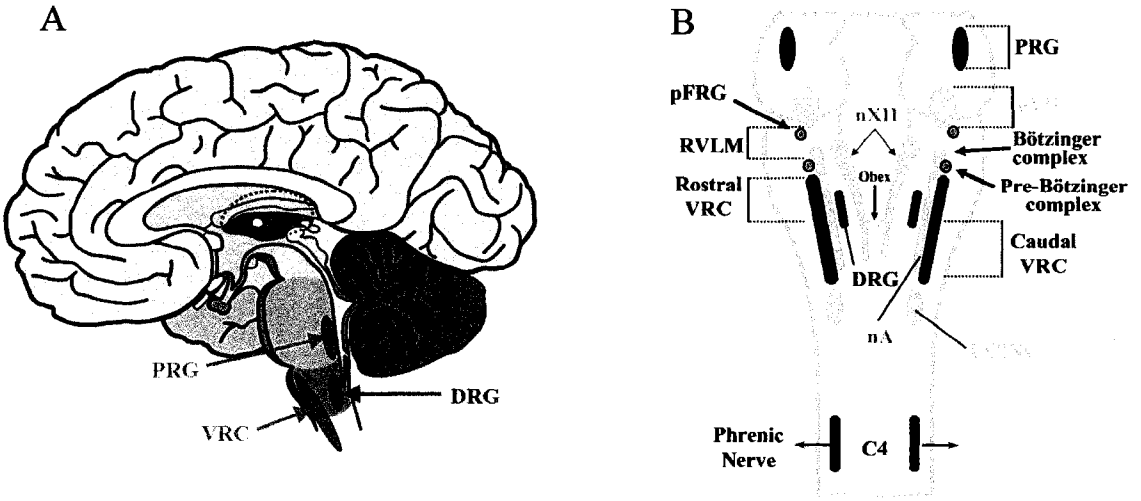


**Figure 1. Schematic representation of the location of the main groups of respiratory neurons** A. Distribution of important respiratory groups in the human brain (sagittal view, modified from www.BrainConnections.com); B. Important respiratory groups involved in respiratory rhythm generation in the mammalian brainstem and spinal cord (coronal view, modified from Duffin, 2004). Abbreviations used: VRC, ventral respiratory column; DRG, dorsal respiratory group; PRG, pontine respiratory group; pFRG, para-facial respiratory group; nVII, facial nucleus; nA, nucleus ambiguus; nXII, hypoglossal nucleus; RVLM, rostral ventrolateral medulla; UCINs, upper cervical inspiratory neurones; C4, corresponding segment of the cervical spinal cord.

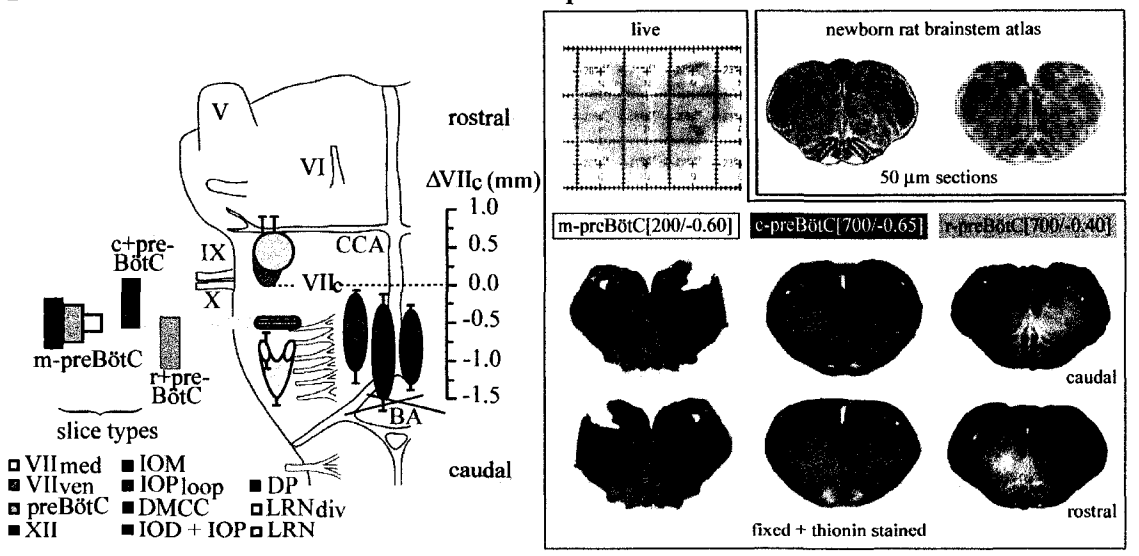


**Figure 2. "Online histology" for the determination of structure-function relationships in physiological (3 mM) [$K^+$] of the isolated pre-Bötzinger Complex (preBötC) inspiratory center.** A, Rostrocaudal extensions of histological marker nuclei for generating rhythmic preBötC slices from postnatal day (P) 0-4 Sprague-Dawley (SD) or Wistar (W) rats. The small standard deviations indicate a high constancy of these nuclei during early postnatal development. The boundaries of rhythmic preBötC slices are identified by the distance (in mm, negative sign indicating caudal location) from the caudal end of the facial nucleus (VIIc) by comparing structures in pre/postrhythmic slices with those in a neonatal rat brainstem atlas (Ruangkittisakul et al., 2006). B (left), photographs of a 200 µm thin slice with the preBötC in the middle ("m-preBötC") showing live slice (top) which was then fixed and thionin-stained after experiment to reveal surface structures (e.g. IO and XII). Middle and right, 700 µm slices containing the preBötC plus either caudal or rostral tissue ("c+preBötC", "r+preBötC" slices), respectively (values in brackets indicate slice thickness in µm and slice boundary in mm). Abbreviations: preBötC, pre-Bötzinger Complex; DMCC, dorsomedial column of inferior olive (IO); IOM, medial IO; IOD, dorsal IO; IOP, principal IO; $IOP_{loop}$, lateral loop of IOP; LRN, lateral reticular nucleus; $LRN_{div}$, LRN divided into medial and lateral subnuclei; $VII_{med}$, medial subnucleus of VII; $VII_{vent}$, ventral subnucleus of VII; XII, hypoglossal nucleus; DP, pyramidal decussation; BA, basilar artery; CCA, caudal cerebellar artery; V,VI,IX,X, trigeminal, abducens, glossopharyngeal, vagal nerves. (From Ruangkittisakul et al., 2007b).

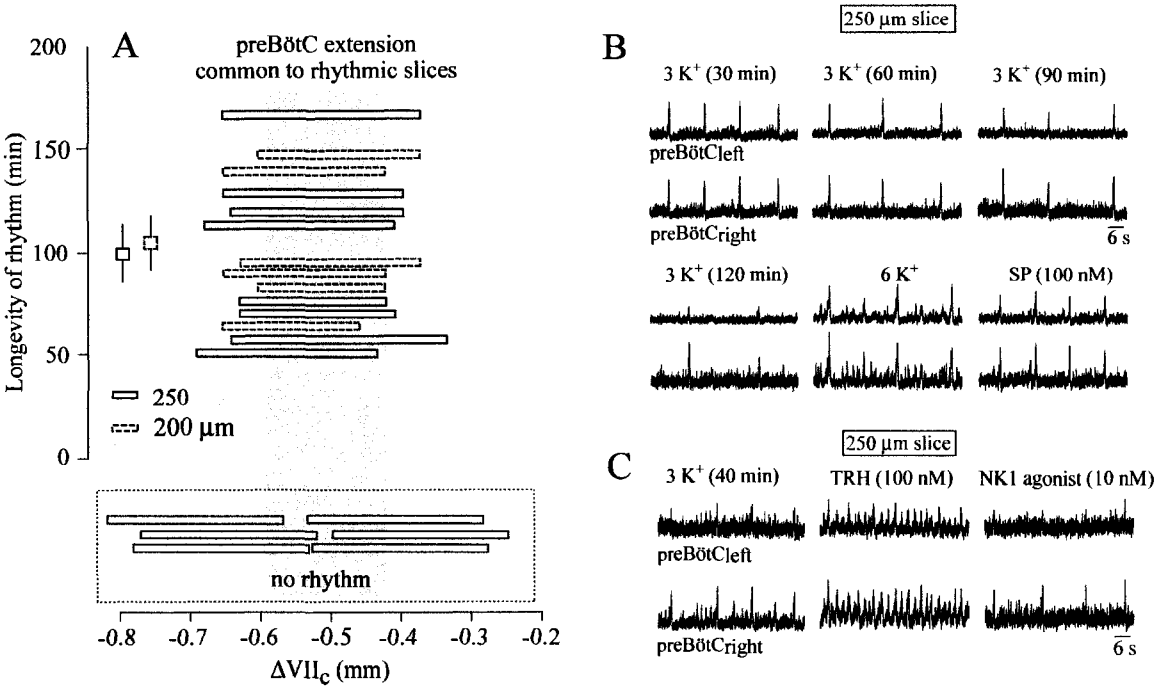


**Figure 3. preBötC boundaries sufficient for rhythm in 3 mM [K$^+$] and properties of 3 mM K$^+$ rhythm in thin slices (200-250 µm).** A, Slice boundaries of 8 m-preBötC[250/-0.65] slices and 6 m-preBötC[200/-0.63] slices. Rectangles with solid and broken lines indicate the mean longevity (plus S.E.M.) of rhythm in the m-preBötC[250] and m-preBötC[200] slices, respectively. 6 m-preBötC[250] slices with boundaries >100 µm deviating from those of rhythmic slices did not show bursting (see box below ΔVIIc scale bar). B, a m-preBötC[250/-0.65] slice showed robust bilaterally-synchronous bursting for >90 min. Regular robust bursts plus smaller amplitude irregular bursts were activated by 6 mM K$^+$ and, subsequently, by substance P. C, Inspiratory pattern in 3 mM K$^+$ of a m-preBötC[250/-0.68] slice was characterized by bilaterally-synchronous robust bursts intermingled with partly synchronous smaller bursts. Following in vitro apnea after 113 min, TRH evoked a fast and synchronous rhythm, whereas subsequent application of the NK1R agonist GR73632 evoked robust bursts of lower rate intermingled with small amplitude bursts. (From Ruangkittisakul et al., 2007b)

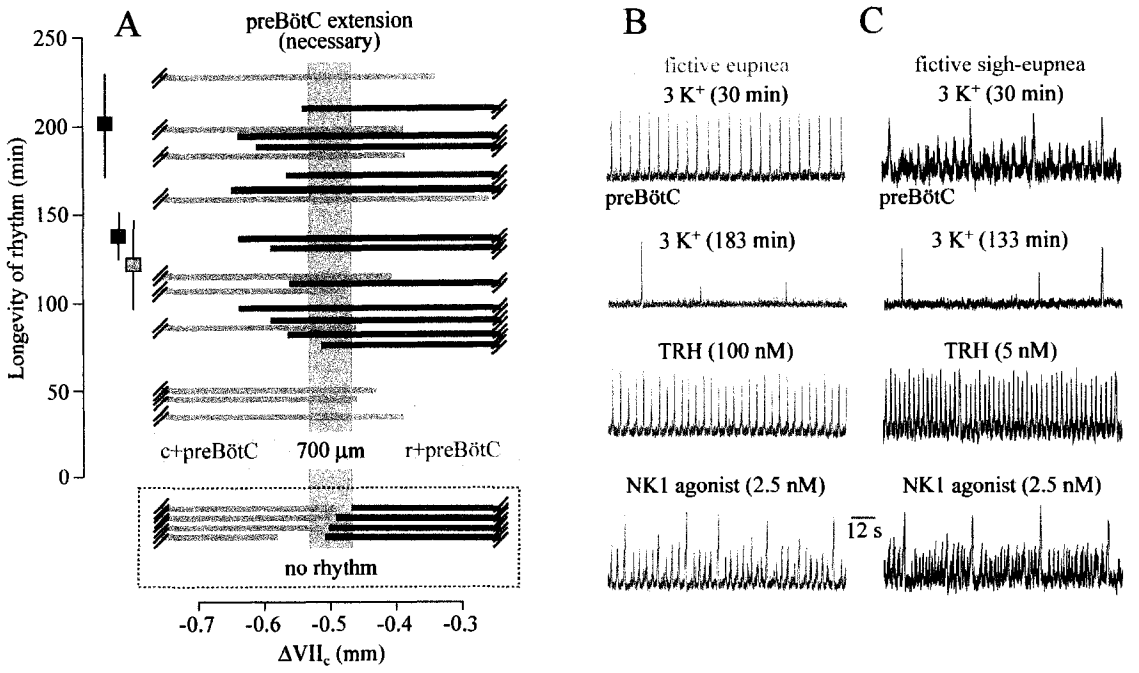


**Figure 4. Boundaries necessary for rhythm in 3 mM $K^+$ and activity patterns of 700 µm thick slices with the preBötC exposed to one surface.** A, Plot of the longevity of rhythm vs. borders of 10 c+preBötC[700/-0.42] slices and 12 r+preBötC[700/-0.58] slices. The preBötC extension necessary for rhythm is possibly <100 µm as indicated by the pink box framing brainstem tissue common to rhythmic slices of both types. The dashed box underneath indicates the boundaries of non-rhythmic slices. The squares next to the longevity scale bar show the mean longevity (and S.E.M.) of rhythms in the 10 c+preBötC[700] (blue square) and the 12 r+preBötC[700] slices (purple square), whereas the black square shows the longevity of rhythm in 7 m-preBötC[700/-0.89] slices. B, The upper panel shows eupnea-like bursts of regular frequency and amplitude in the c+preBötC. Following the occurrence of in vitro apnea ~2 min after the recording in the 2$^{nd}$ panel from top, consecutive bath-application of TRH (middle panel) and the NK1R agonist GR73632 (bottom panel) reactivated eupnea- and sigh-like rhythms, respectively. C, The upper panel shows sigh-like large bursts and smaller amplitude intersigh bursts in the r+preBötC slice. In vitro apnea occurring ~3 min after the recording in the 2$^{nd}$ panel from top was reversed into regular, eupnea-like rhythm by TRH (middle panel), whereas GR73632 initiated a sigh-like rhythm very similar to that in control (bottom panel). (From Ruangkittisakul et al., 2007b)

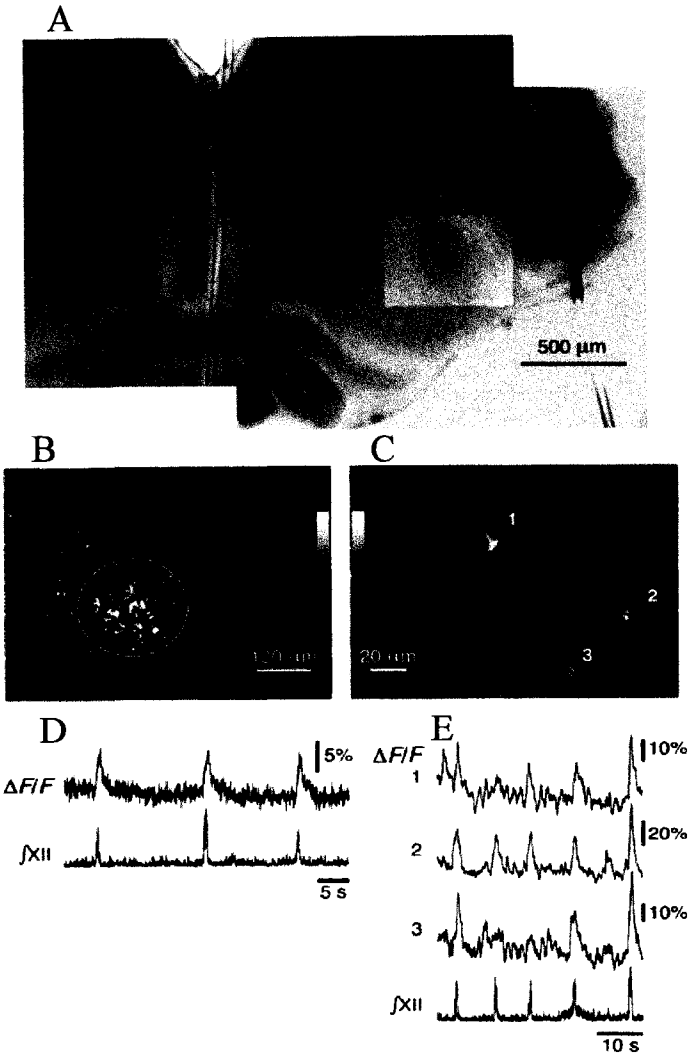


**Figure 5. Calcium Green-1 AM (CaG) injection site and localized $Ca^{2+}$ activity in the preBötC** A, Image of slice with fluorescence (pseudocolour) showing CaG retrograde labelling after 12 h (highlighted rectangle). B, Inspiratory 'flash' image in highlighted rectangle in A. C, High magnification flash image of region in B showing individual inspiratory neurons in a single focal plane (neuron somata labelled 1–3). D, Rhythmic elevations in fluorescence intensity (ΔF/F) in the circular area in B, and (E) in individual neurons (modified from Koshiya and Smith, 1999)

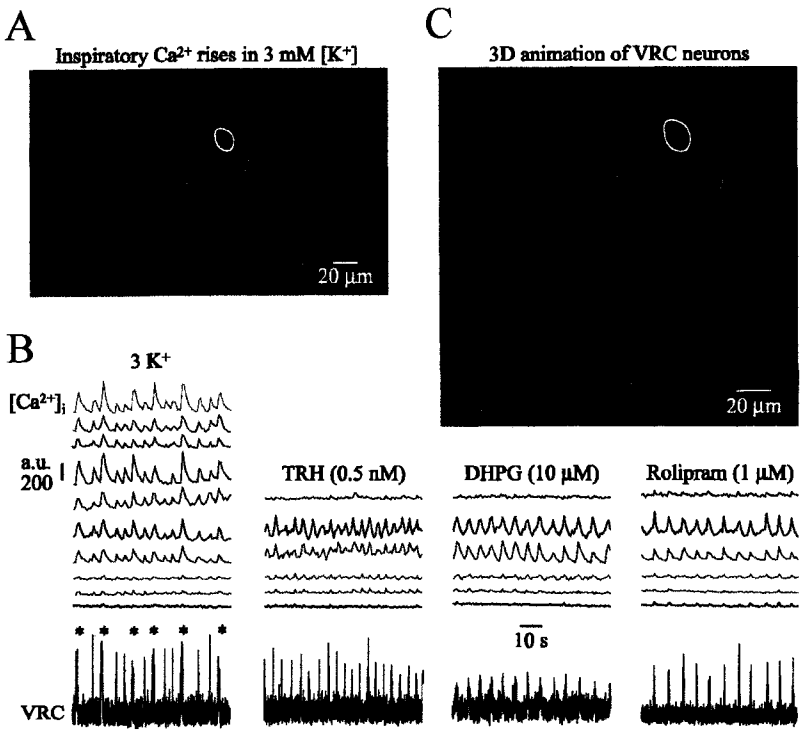


**Figure 6. Confocal imaging of activity and morphology of inspiratory VRC neurons.** A, Cells in the VRC region of mPBC[500/–0.75] slice stained after pressure injection with the $Ca^{2+}$ sensitive dye Fluo-4-AM, located at a depth of 30 µm (i.e., –0.72 mm caudal to VIIc). B, simultaneous recordings in 3 mM [$K^+$] of rhythmic $Ca^{2+}$ oscillations plotted as fluorescence intensity in arbitrary units (a.u.) in identified VRC neurons in A and electrophysiological population activity in the contralateral VRC (bottom trace). Astersiks indicate intermingled bursts associated with larger $Ca^{2+}$ rise. After washout of rhythm in 3 mM [$K^+$], VRC bursting and $Ca^{2+}$ oscillations were reactivated by TRH, 3,5-dihydroxy-phenylglycine (DHPG), or the blocker of cAMP-dependent phosphodiesterase 4, rolipram. C, 3D animation showing gross morphology of VRC inspiratory neurons and nonrhythmic cells obtained from z-stack image series encompassing areas starting 7.5 µm above to 7.5 µm below the image plane of A. (From Ruangkittisakul et al., 2006)

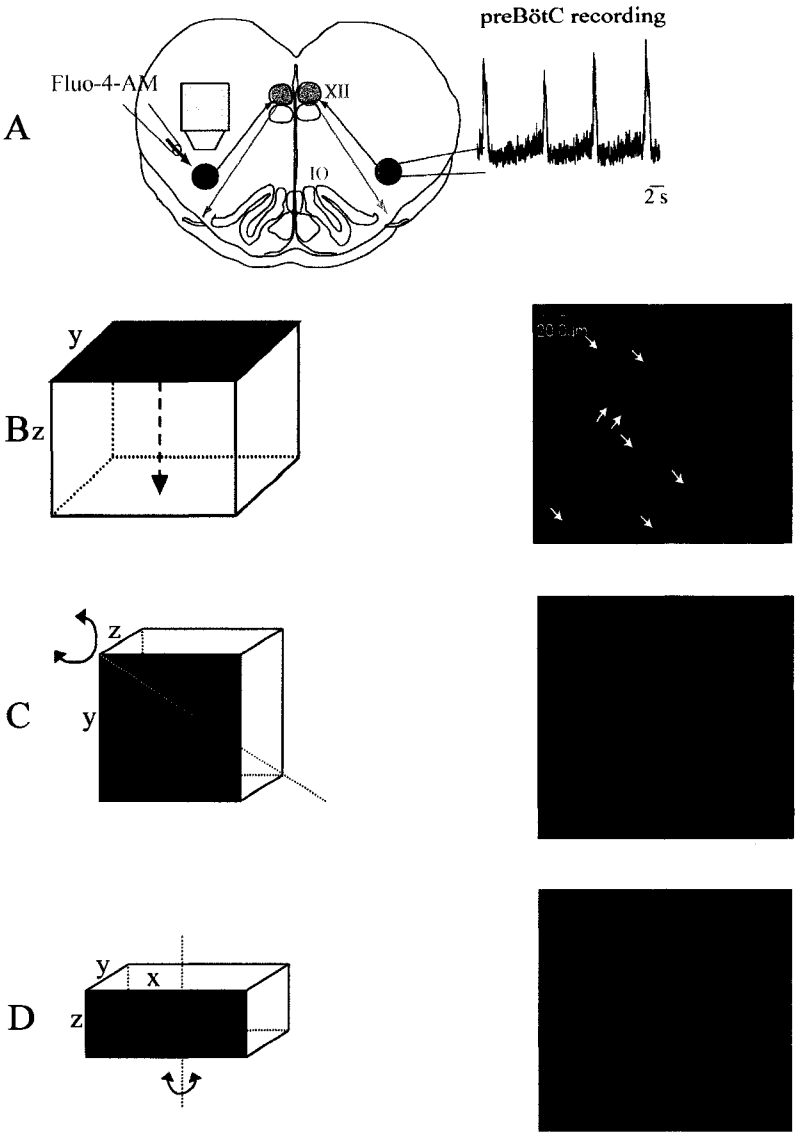


**Figure 7. Diagram of the methodological approach used for extracellular recordings and multiphoton/confocal $Ca^{2+}$ imaging.** A, Transverse medullary slices were used for extracellular recordings (right side: suction electrodes positioned at the level of preBötC to record neuronal population activity) and multiphoton/confocal $Ca^{2+}$ imaging (left side: Fluo-4-AM was injected with a broken patch pipette into the preBötC and stained cells were imaged using multiphoton/confocal microscopy). B, (left panel) diagram of z-stack measurement showing the progressive scanning of xy-plane images along the z-axis, and (right panel) summation these planes to reveal a 3D image. C, schematic and image of 3D generated from a z-stack showing rotation in x- and y-axes. D, diagram and image of xz-plane image rotated along the z-axis showing the lateral view of the stained area.

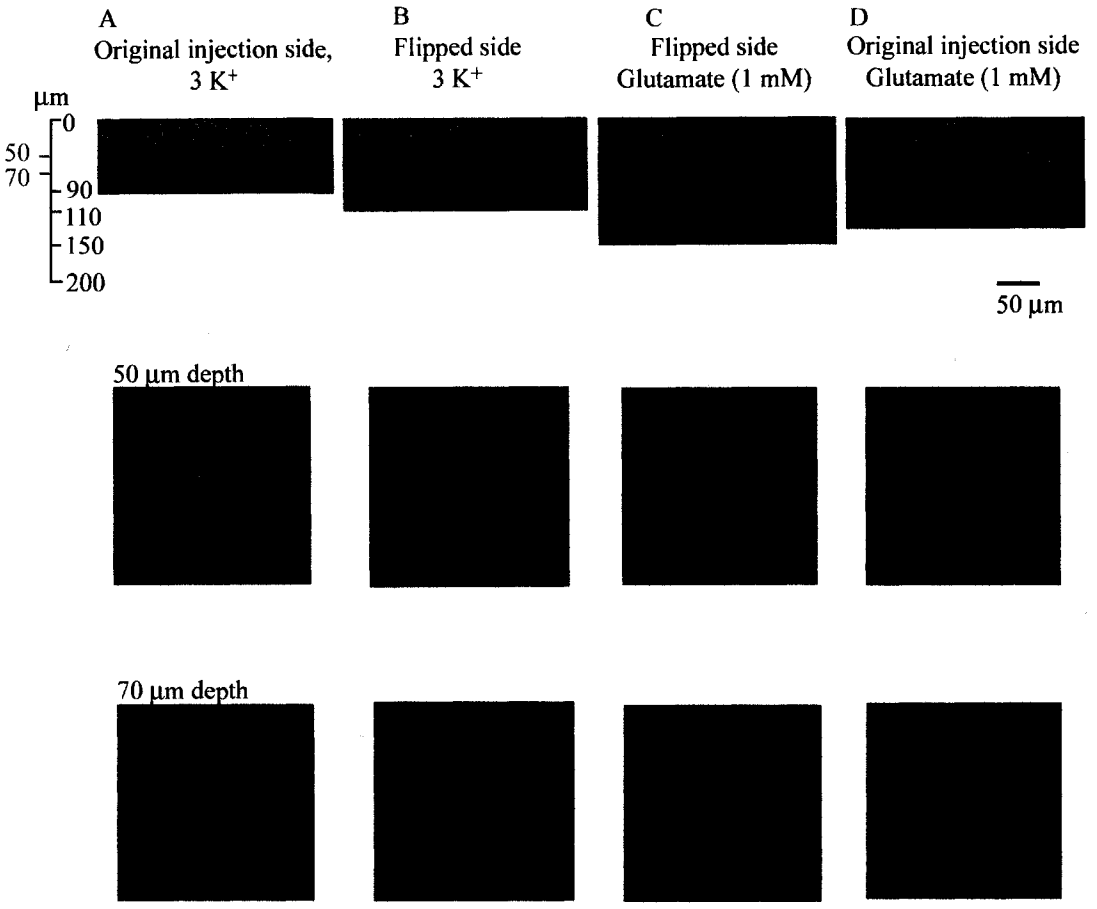


**Figure 8. Comparison of staining depths at the original injection site and on the opposite side in thin slices (multiphoton microscopy).** A, reconstruction in lateral view (xz plane) of the z-stack performed in a 200 µm brainstem slice showing the extent of Fluo-4-AM staining as recorded from the original injection site in 3 mM [$K^+$] superfusate. Neurons were stained up to a depth of 90 µm although morphological details were lacking at deeper levels (compare images at 50 µm and 70 µm depths). B, slice was flipped to see the extent of staining from the surface opposite to injection site. Superficial layers showed unspecific staining while neurons became apparent at 50-70 µm depth. Bath-application of glutamate (1mM) improved visibility of neurons (compare A, D, at original injecting site, and B, C, on flipped side).

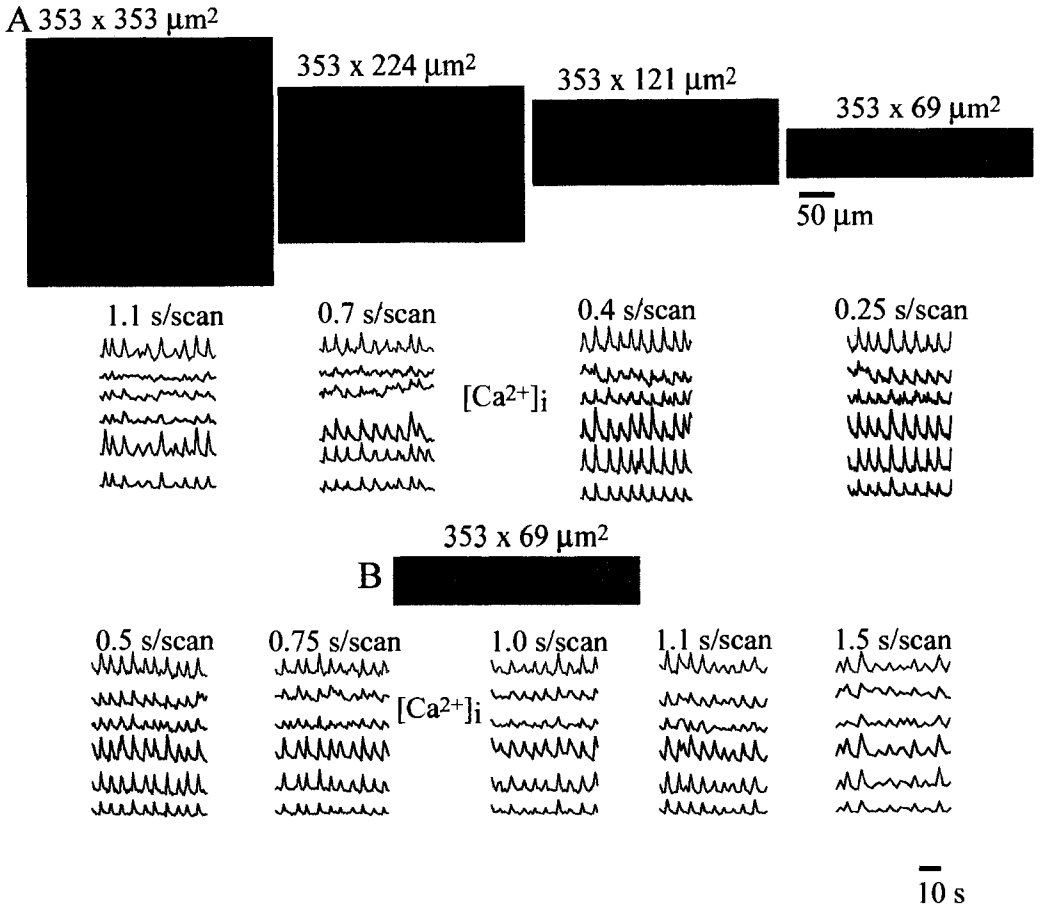


**Figure 9. Temporal resolution of inspiratory $Ca^{2+}$ oscillations.** A, Fluo-4-AM fluorescence signals measured from regions of interest (ROIs) outlining cell bodies of VRC cells located 50 μm into a m-preBötC[550/-0.75] slice showed inspiratory $Ca^{2+}$ oscillations in 5 mM $K^+$ superfusate. Each fluorescence trace was a measurement from a single cell. 1.1 s/scan rate in full mode (353 x 353 $\mu m^2$) revealed some missing peaks in the fluorescence traces. Increasing the scan rate by clipping the image size to 0.7 s/scan resulted in well-resolved peak amplitudes. Faster scan rates (0.4-0.25 s/scan) at a more reduced image size increased peak amplitude slightly. B, Scanning clipped image (353 x 69 $\mu m^2$, 0.25 s/scan) with increasing resting periods resulted in decreased temporal resolution. At 1.0 s/scan (0.25 s scanning time plus 0.75 s resting time), some fluorescence peaks started to reduce in amplitude. At 1.5 s/scan (0.25 s scanning time plus 1.25 s resting time), 50 % of the peaks could not be resolved.

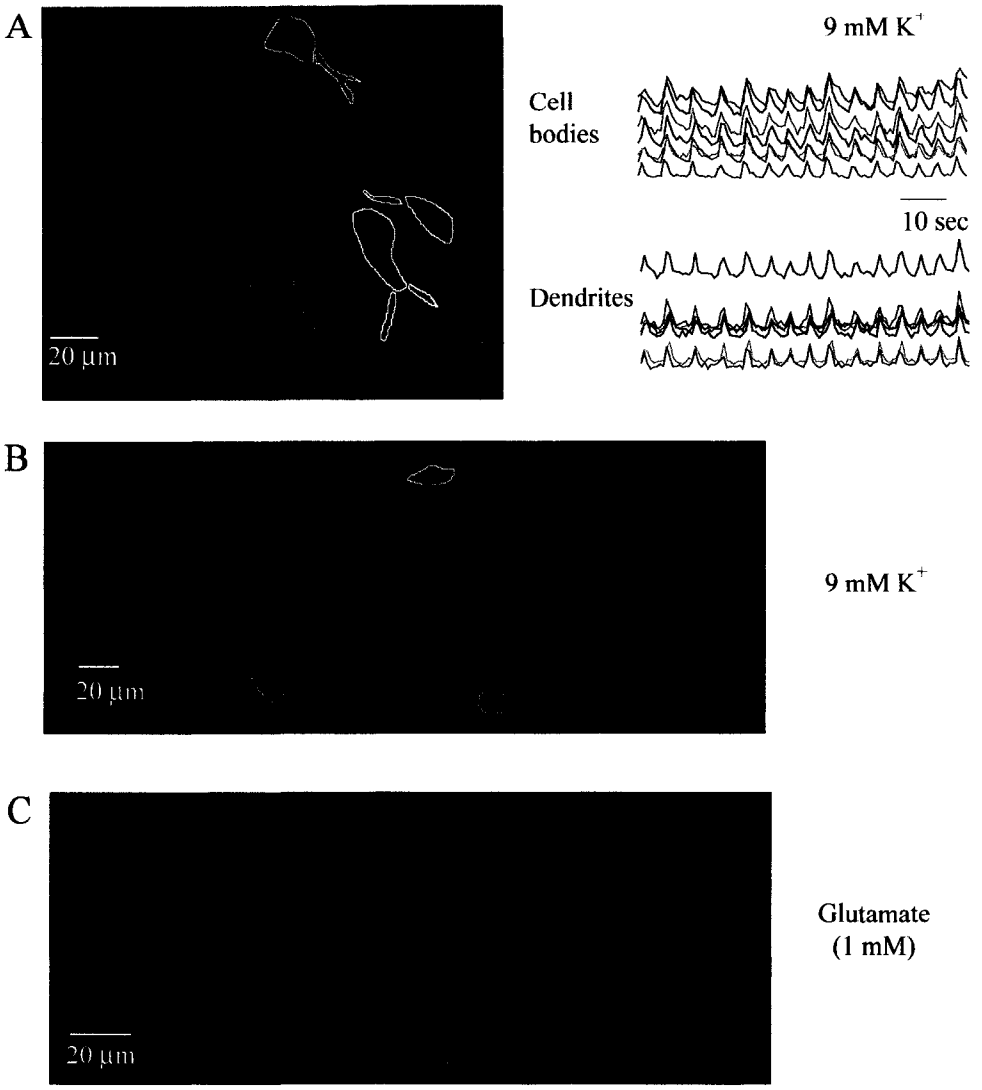


**Figure 10. Inspiratory $Ca^{2+}$ oscillations of preBötC cells imaged in 9 mM $K^+$ superfusate and glutamate (1 mM) solution.** A, Cells at -0.56 in a r+preBötC[700/-0.61] slice showed rhythmic oscillations of somata and proximal dendrites; B, z-stack summation of inspiratory preBötC cells imaged in 9 $K^+$, measured 8.5 µm above and below the level of the cells located at -0.58 in a r+preBötC [700/-0.63] slice; C same cells as in B, z-stack performed during glutamate (1 mM) application. Note the improved visualization of cell somata and proximal dendrites.

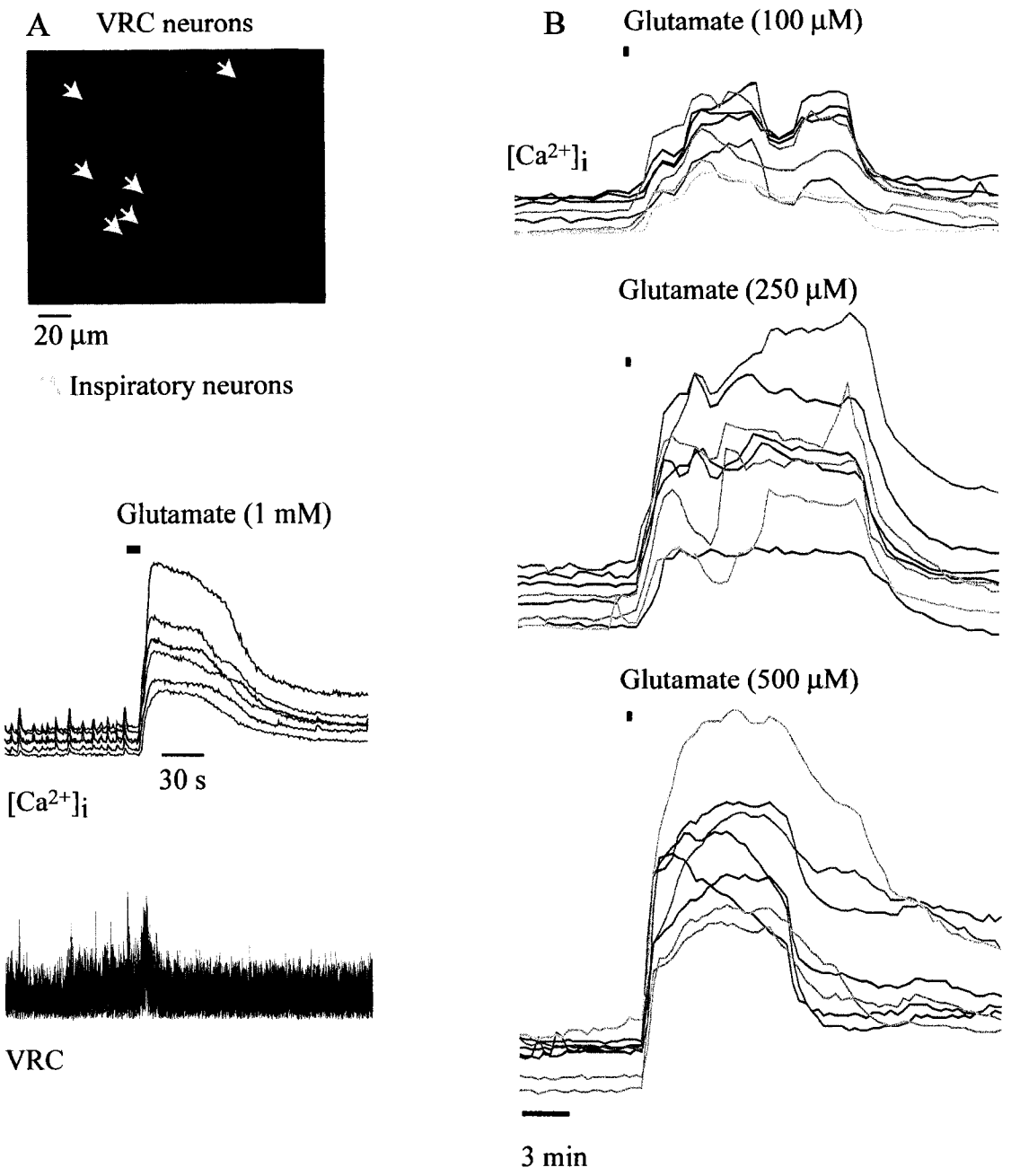


**Figure 11. Effects of glutamate on the amplitude of inspiratory $Ca^{2+}$ oscillations.** A, Bath application (10 s) of glutamate (1 mM) produced an increase of Fluo-4-AM fluorescence intensity in inspiratory VRC cells which was 3-10 times larger than the spontaneous inspiratory $Ca^{2+}$ oscillations; B. Bath application (30 s) of 100-250 μM glutamate produced variable effects whereas only 500 μM produced strong, steady increases in Fluo-4-AM fluorescence, similar to the effect seen with 1 mM glutamate.

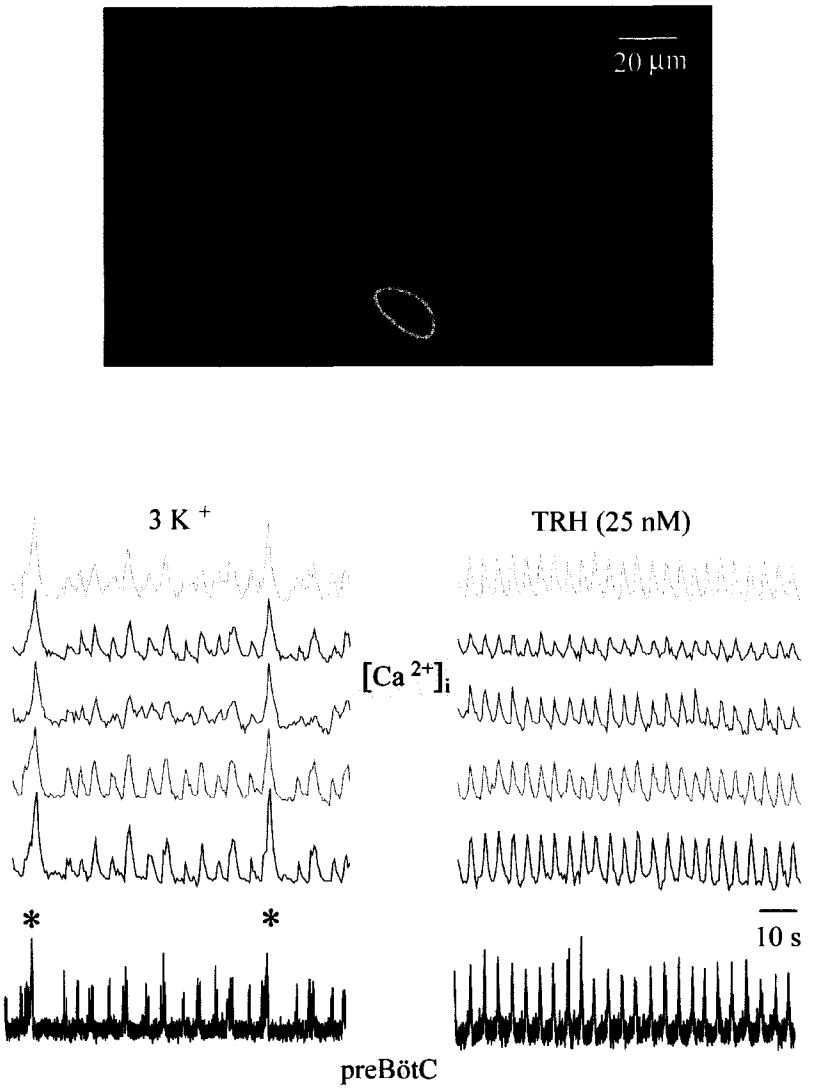


**Figure 12. Reconfiguring activity patterns of inspiratory preBötC neurons visualized with multiphoton-imaging of cytosolic [$Ca^{2+}$] rises.** $Ca^{2+}$ rises of preBötC neurons located 25 µm caudal to the preBötC center occur simultaneously with contralateral preBötC neuronal population activity recorded electrophysiologically from a r+preBötC[700/-0.58] slice. Bath-applied TRH transformed both the inspiratory optical and electrophysiological pattern with two sighs (asterisks) and various intersigh bursts into eupnea-like regular activities. (From Ruangkittisakul et al., 2007b)

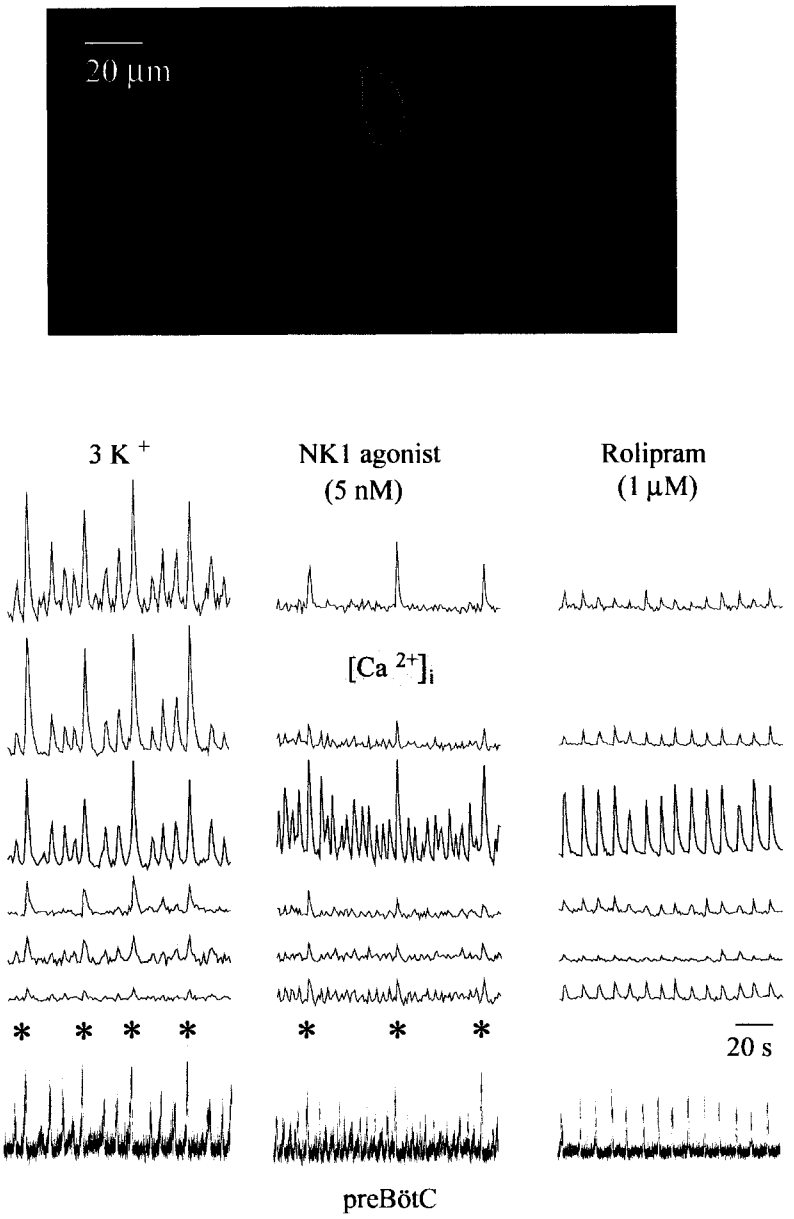


**Figure 13. NK1R agonist reactivates sighs whereas rolipram reconfigures the pattern to eupnea.** The size of larger amplitude sigh (asterisks) and smaller amplitude intersigh bursts recorded electrophysiologically from a r+preBötC[700/-0.60] slice was reflected in the amplitude of $Ca^{2+}$ oscillations in preBötC neurons located 60 μm caudal to the preBötC center. After spontaneous in vitro apnea, sigh-like activities were reactivated by the NK1R agonist GR73632, whereas rolipram reactivated eupnea-like signals after washout of NK1R agonist. (From Ruangkittisakul et al., 2007b)

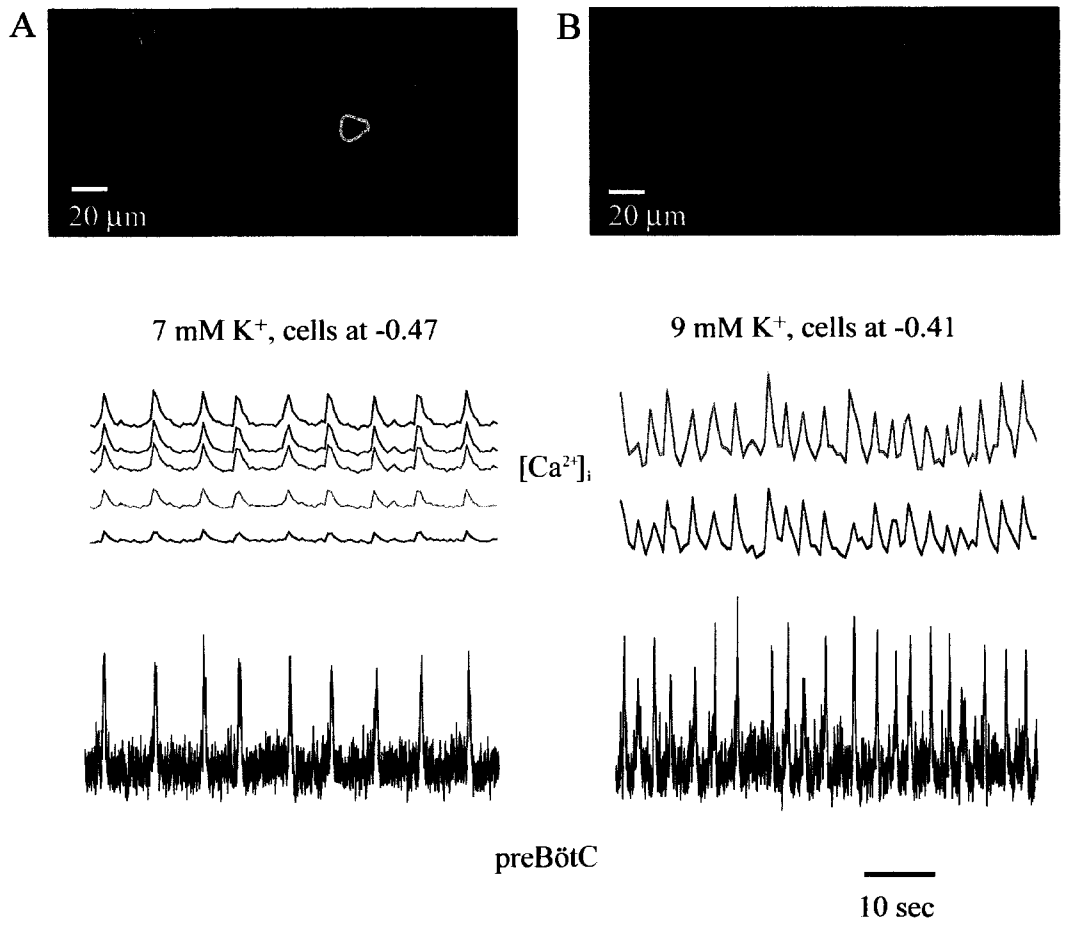


**Figure 14. $Ca^{2+}$ oscillations of inspiratory neurons imaged in c+preBötC slices.** Active cells were apparent mainly in high $K^+$ superfusate and their number was lower compared with neurons imaged in r+preBötC slices (A, cells at 0.47 mm caudal to $VII_c$ in a c+preBötC [700/-0.42] slice, imaged in 7 mM $K^+$; B, cells at 0.41 mm caudal to $VII_c$ in another c+preBötC [700/-0.45] slice, imaged in 9 mM $K^+$). Time scale applies for both panels.

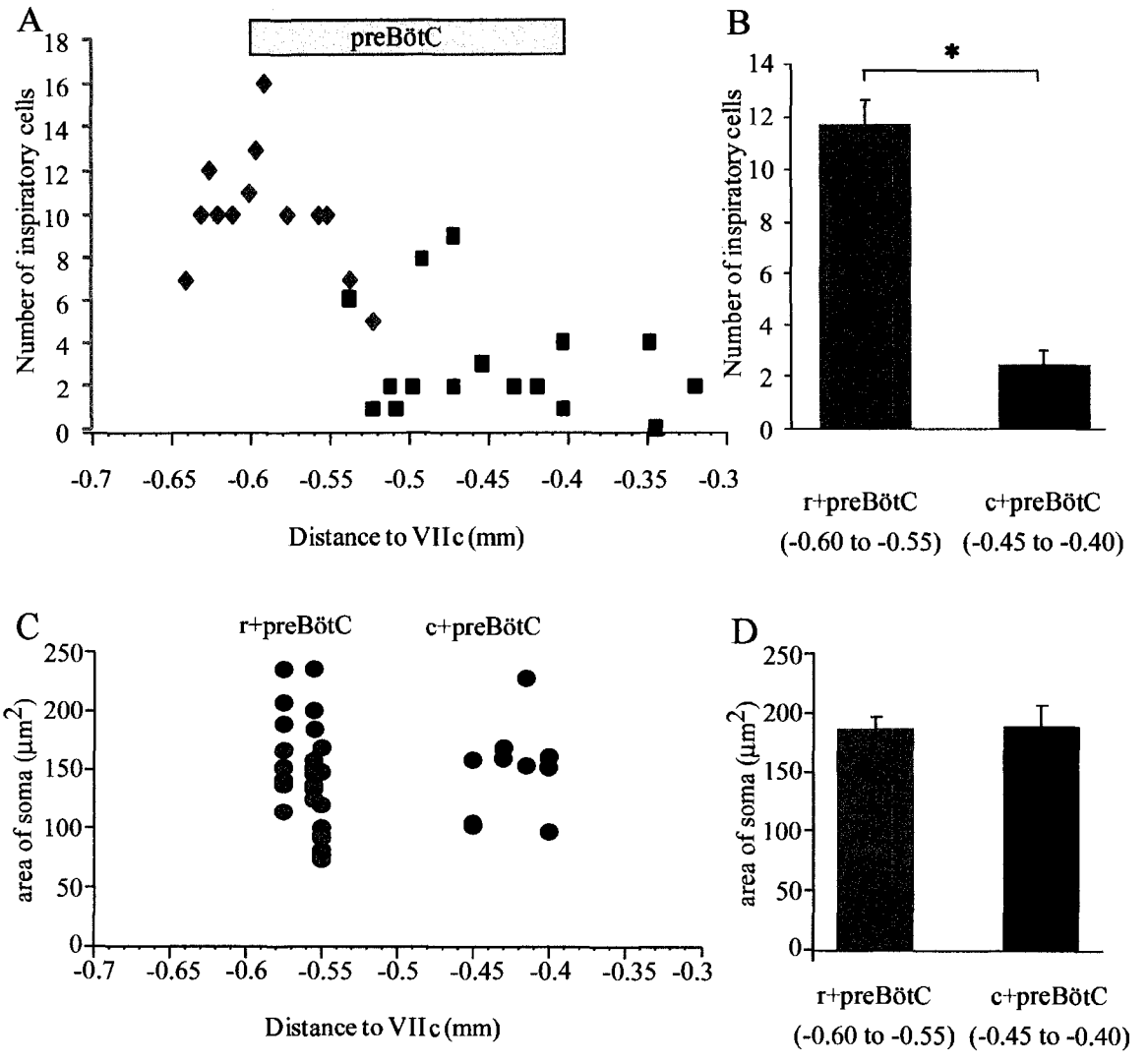


**Figure 15. Comparison of number and size of inspiratory cells imaged in r+preBötC versus c+preBötC slices.** A, Plot of inspiratory preBötC cells number imaged in r+preBötC slices (pink) and c+preBötC slices (blue). Each dot represents the number of active cells that were measured at different rostrocaudal levels referred to $VII_c$ (7 r+preBötC, mean caudal border at -0.62±0.02 caudal to $VII_c$, and 12 c+preBötC, mean rostral boundary at 0.42±0.03 mm caudal to $VII_c$). B, In 5 r+preBötC slices and 5 c+preBötC slices, the number of active cells located on the caudal (-0.60 to -0.55) versus rostral (-0.45 to -0.40) border of the preBötC was averaged and showed a significant difference (one sample t-test, $p < 0.05$). C, Plot of soma size of active neurons imaged on the caudal and rostral boundaries of the preBötC versus the distance to $VII_c$. The soma size ranged from 73 to 235 $\mu m^2$ at caudal preBötC border (0.60-0.55 mm to $VII_c$, in 3 r+preBötC slices) and from 96 to 227 $\mu m^2$ at rostral preBötC border (0.45-0.40 mm to $VII_c$, in 5 c+preBötC slices) respectively. D, Plot of the average soma size showing no significant difference in cell size between inspiratory active neurons at the caudal and rostral preBötC borders ($p > 0.05$).

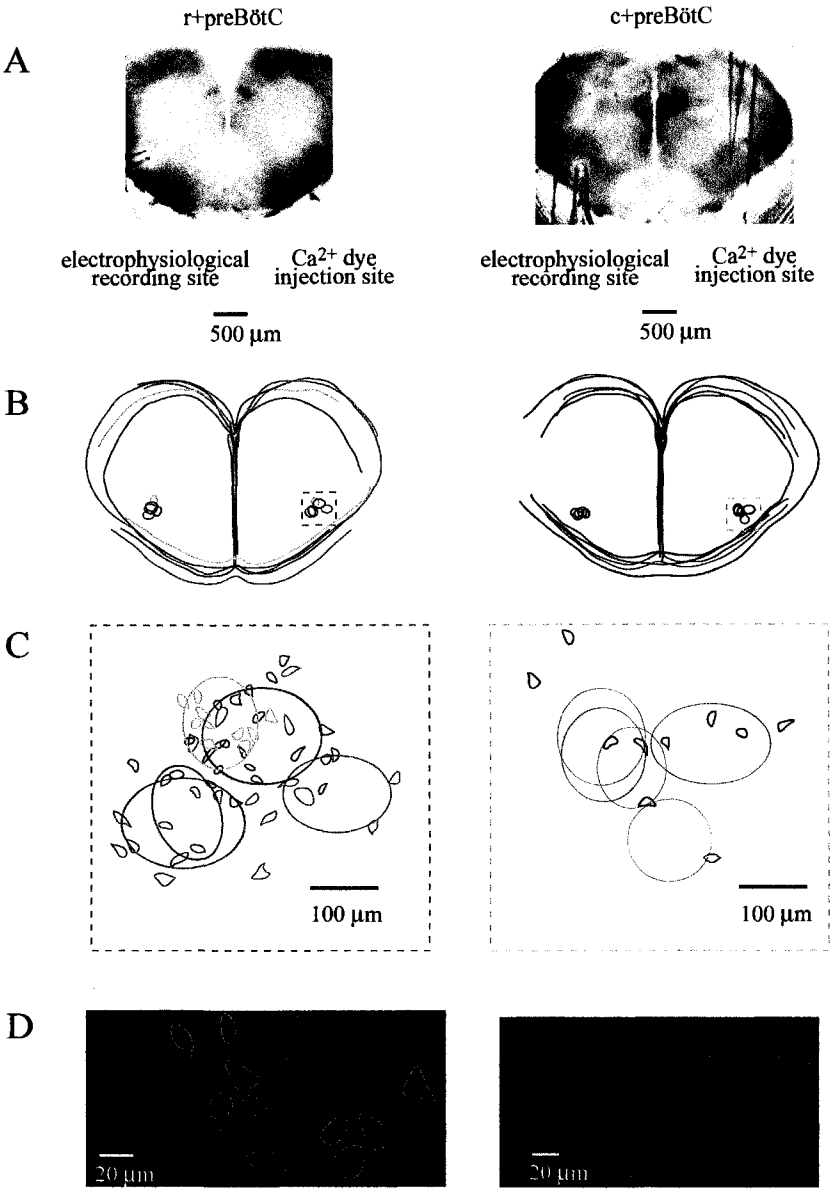


**Figure 16. Distribution diagram of inspiratory cells imaged in r+preBötC versus c+preBötC slices.** A, Examples of transmitted light images captured with low magnification objective (4x) used to obtain the distribution diagram. B, outlines of slice and its recording/injection sites from 5 r+preBötC[700/-0.62] and 5 c+preBötC[700/-0.41] slices were overlapped at the slice center and showed symmetrical location of electrophysiological recording and $Ca^{2+}$ dye injection sites. C, combining ROIs of inspiratory active cells and their corresponding injection site suggested a "clustered" localization of these neurons at the caudal border of the preBötC, contrasting with a dispersed arrangement of inspiratory neurons at the rostral border of the preBötC. D, 3D summation of z-stack measured 10 µm and 8.5 µm respeectively above and below the plane of measured cells (left: cells at 0.58 mm caudal to $VII_c$ in a r+preBötC[700/-0.62] slice, right: cells at 0.46 mm caudal to $VII_c$ in a c+preBötC[700/-0.41] slice).

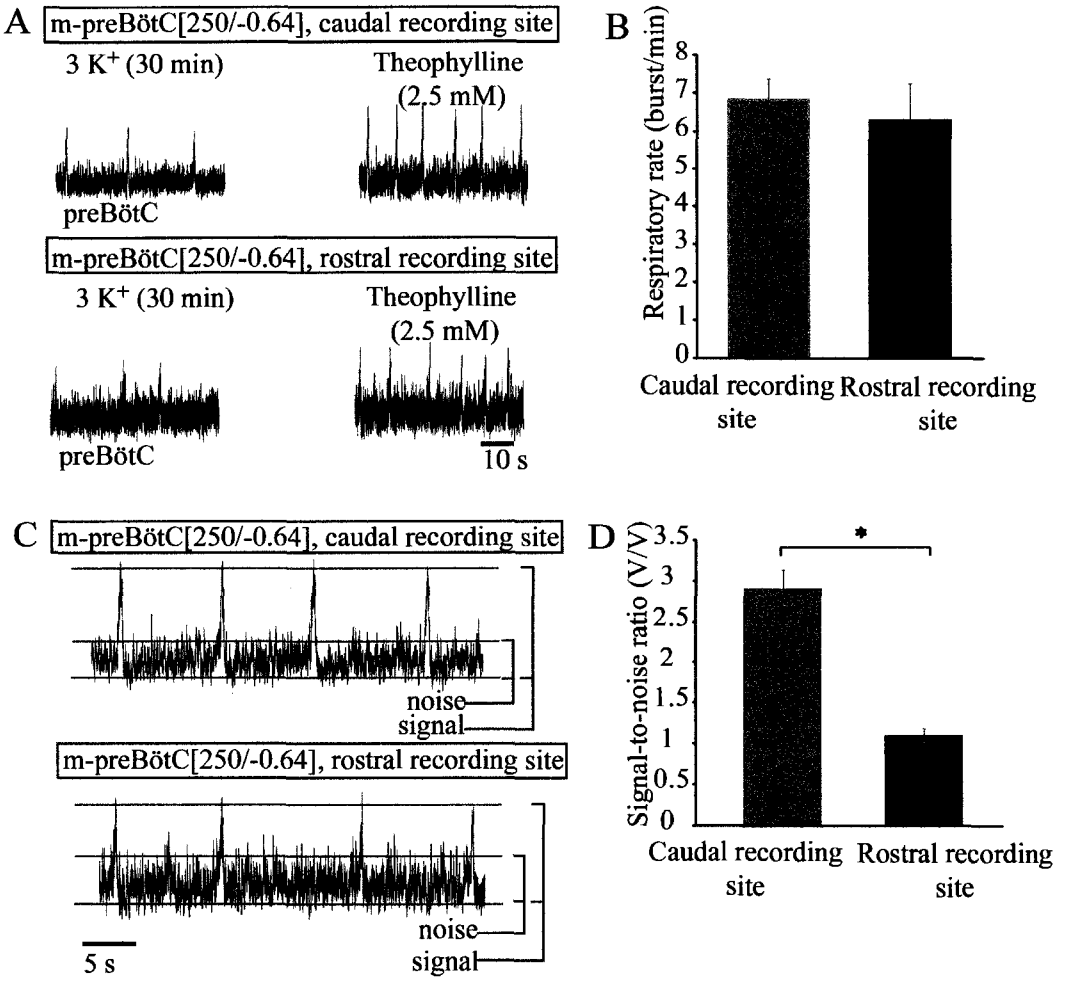


**Figure 17. Stimulatory effect of theophylline (2.5 mM) on inspiratory rhythm recorded from caudal and rostral sides of thin m-preBötC[250/-0.64] slices.** A, preBötC population activity recorded from caudal and rostral aspects of m-preBötC[250/-0.64] in 3 mM $K^+$ and theophylline (2.5 mM). Theophylline elicited a regular, robust rhythm on both sides of the thin slices. B, Theophylline had a similar stimulatory effect on inspiratory burst rate recorded from caudal (n=5) and rostral (n=5) sides of thin slices ($p > 0.05$). C, Evaluation of signal-to-noise ratio for electrophysiological recordings on caudal and rostral aspects of m-preBötC[250/-0.64]. Red lines represent the approximate levels of baseline (lowest), noise (middle) and peak of inspiratory burst (highest). D, Signal-to-noise ratio was averaged for caudal side recordings (n=6) and rostral side recordings (n=6) during bath-application of theophylline revealing a significantly lower signal-to-noise ratio for the rostral side recordings ($p < 0.05$).

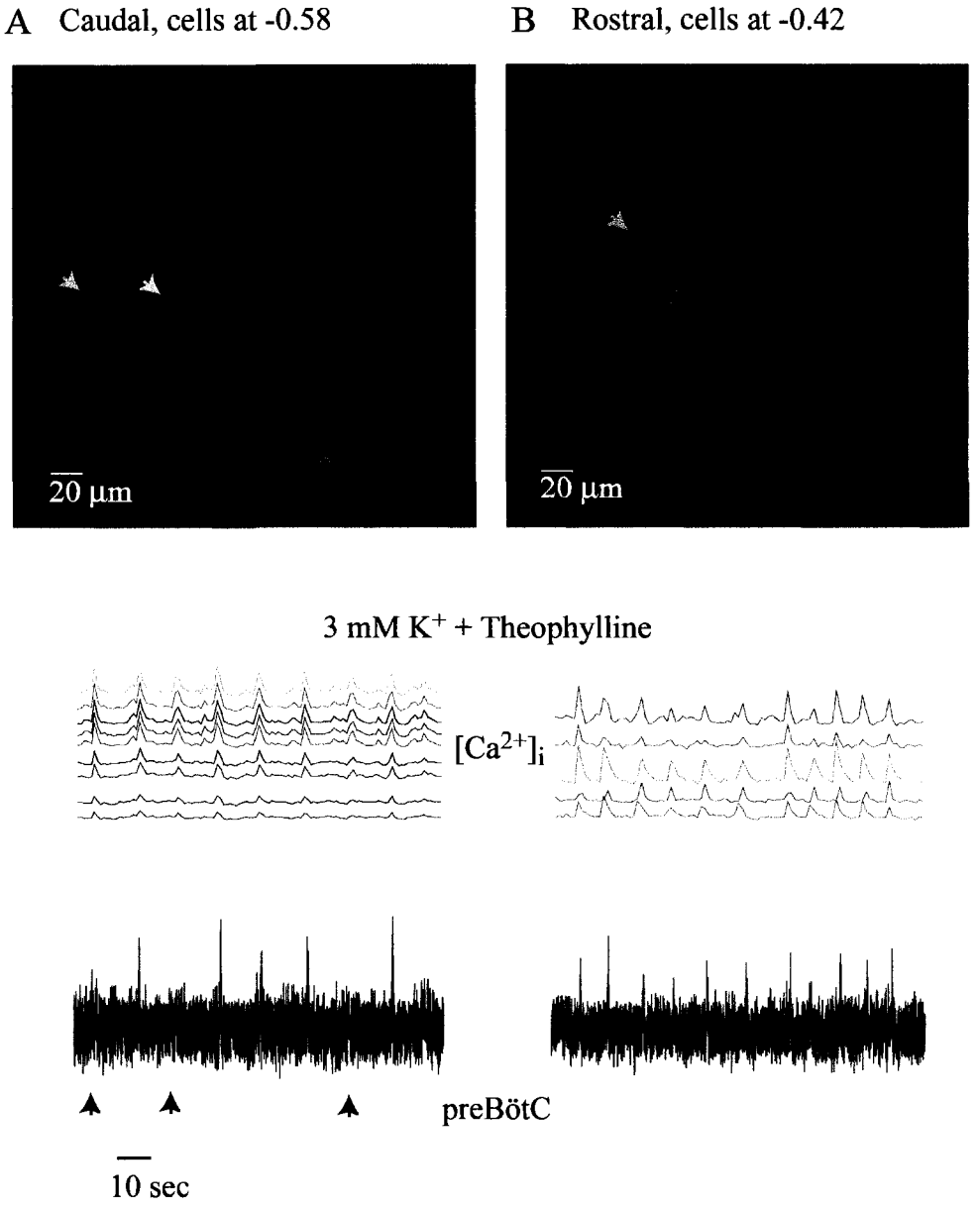


**Figure 18. Inspiratory $Ca^{2+}$ oscillations measured on caudal and rostral sides of m-preBötC[250].** A, preBötC neurons imaged on the caudal side of the thin slice (cells at -0.58 mm to $VII_c$ in m-preBötC[250/-0.64]. Compared to $Ca^{2+}$ oscillations, preBötC population recording showed slower burst rate. During the skipped bursts, there was an increase in baseline noise in the population recording. B, preBötC neurons imaged on the rostral side of the thin slice (cells at -0.42 mm to $VII_c$ in a m-preBötC[250/-0.64] slice with the rostral border at -0.37 mm to $VII_c$). Both recordings were performed in theophylline (2.5 mM).

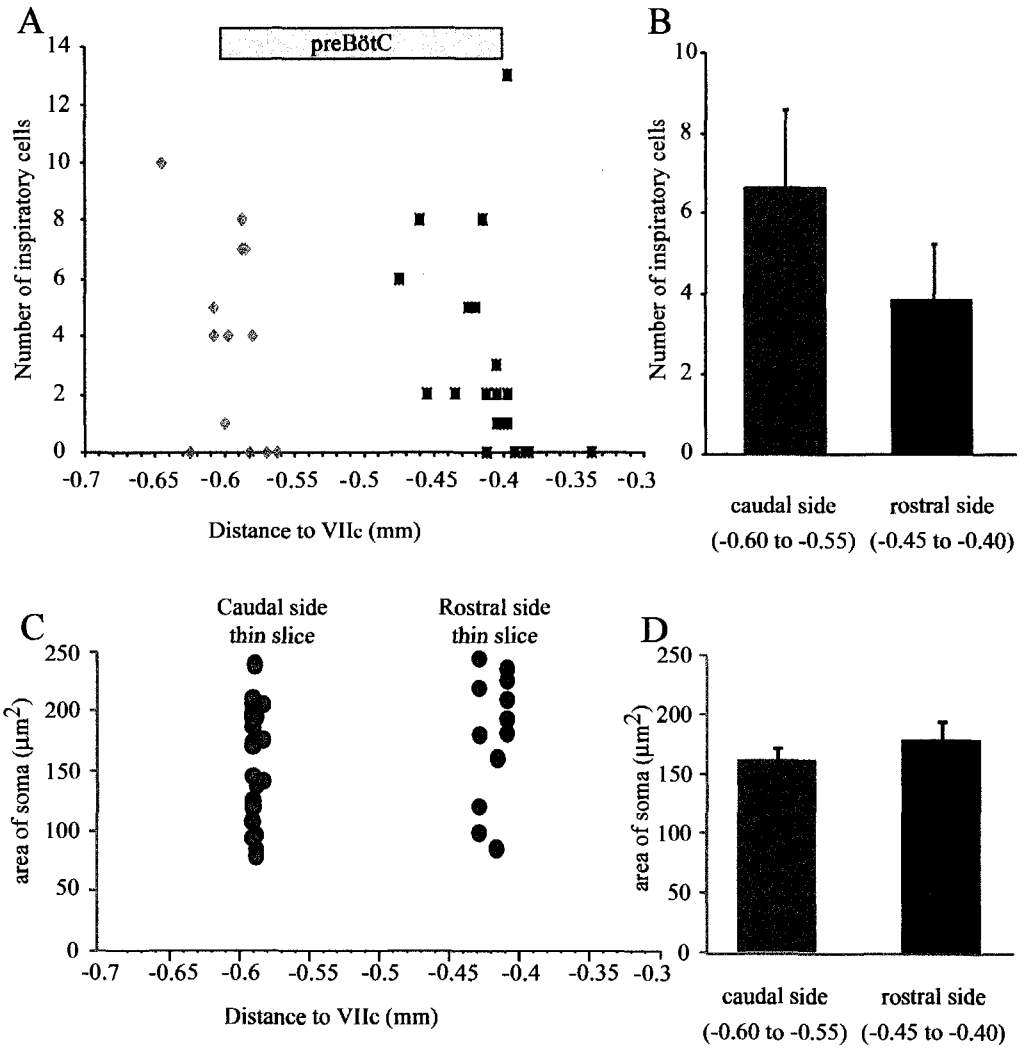


**Figure 19. Comparison of number and size of inspiratory cells imaged on caudal and rostral aspects of thin slices during application of theophylline.** A, Scatter plot of inspiratory cells on the caudal (pink) and rostral (blue) sides of m-preBötC[250/-0.64]. Each dot represents the number of active cells that were measured at different rostrocaudal levels referred as distance to $VII_c$. The number of active cells imaged on caudal and rostral aspects of thin slices showed similar values. B, Average number of inspiratory cells on the caudal (between 0.60 and 0.55 mm caudal to $VII_c$) versus rostral (between 0.45 and 0.40 mm caudal to $VII_c$) border of the preBötC. One sample t-test did not show a significant difference ($p > 0.05$). C, Plot of soma size of active neurons imaged on the caudal and rostral sides of the thin preBötC slices versus the cell location calculated as distance to $VII_c$. The soma size of imaged cells ranged from 78 to 248 $\mu m^2$ at the caudal preBötC border (measured in 3 thin preBötC slices) and from 98 to 243 $\mu m^2$ at rostral preBötC border (measured in 3 thin preBötC slices) respectively. D, Plot of the average soma size of inspiratory cells located at the borders of preBötC (between 0.60 and 0.55 caudal to $VII_c$ on the caudal aspect of thin preBötC slices and between 0.45 and 0.40 caudal to $VII_c$ on the rostral aspect of thin preBötC slices). There was no significant difference in cell size between these two populations ($p > 0.05$).

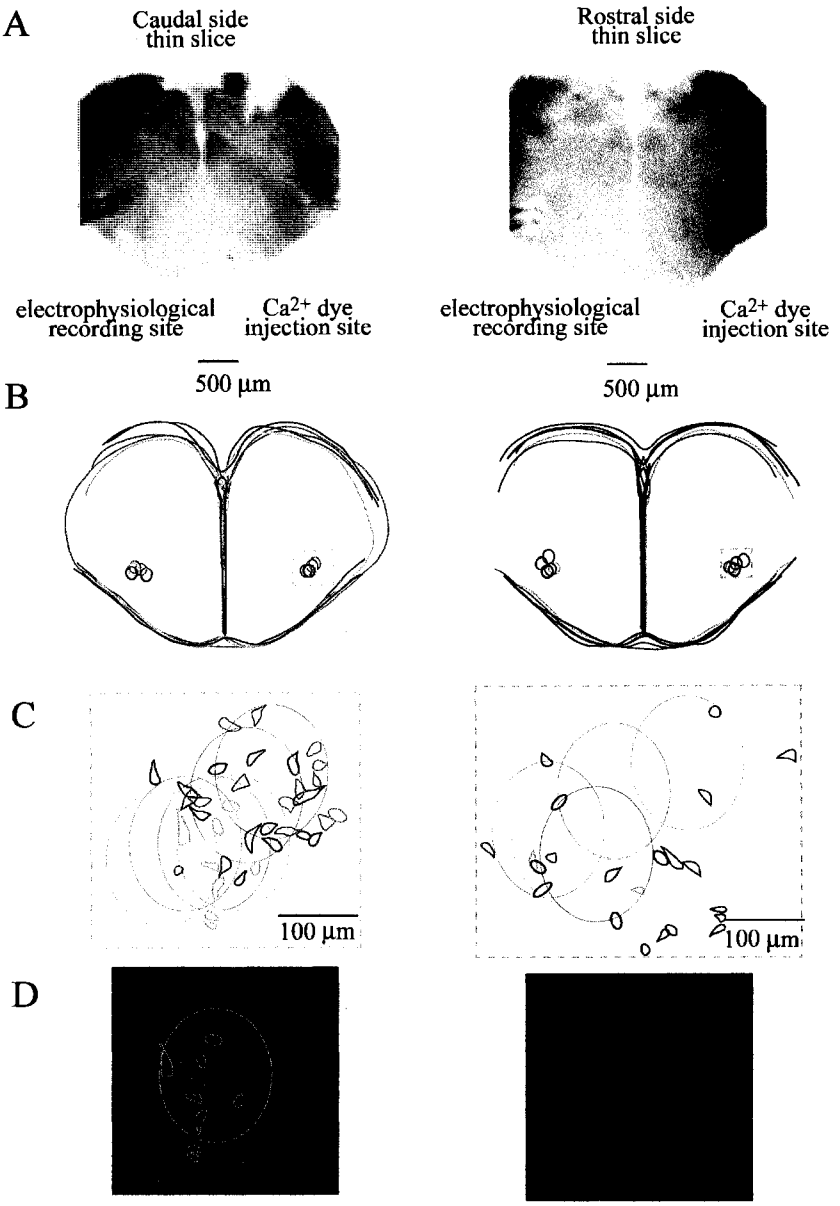


**Figure 20. Distribution diagram of active cells imaged on the caudal versus rostral side of m-preBötC[250] slices.** A, Examples of transmitted light images of thin slices used for $Ca^{2+}$ imaging experiments on the caudal side and rostral side, respectively, captured with low magnification objective (4x). B, The diagram obtained by overlapping outlines of slice and its recording/injection site (5 m-preBötC[250/-0.64] slices for caudal recording site and 5 m-preBötC[250/-0.64] slices for rostral recording site) at the slice center showed consistent location of electrophysiological recording and $Ca^{2+}$ dye injection sites on both sides. C, combining ROIs of inspiratory active cells and their corresponding injection site suggested a "grouped" organization of these neurons at the caudal border of the preBötC, whereas on the rostral border the distribution of inspiratory neurons was more dispersed. D, Inspiratory cells located at 0.6 mm caudal to $VII_c$ imaged on the caudal aspect of a thin slice and 0.42 mm caudal to $VII_c$ imaged on the rostral aspect of a thin slice.

# 7. References


Alheid GF, Milsom WK, McCrimmon DR (2004) Pontine influences on breathing: an overview. Respir Physiol Neurobiol 143:105–114.

Ballanyi K, Onimaru H, Homma I (1999) Respiratory network function in the isolated brainstem-spinal cord of newborn rats. Prog Neurobiol 59:583-634.

Barnes BJ, Tuong CM, Mellen NM (2007) Functional imaging reveals respiratory network activity during hypoxic and opioid challenge in the neonate rat tilted sagittal slab preparation. J Neurophysiol 97:2283-2292.

Bhatia J (2000) Current options in the management of apnea of prematurity. Clin Pediatr (Phila) 39:327-336.

Bianchi AL, Denavit-Saubie M, Champagnat J (1995) Central control of breathing in mammals: neuronal circuitry, membrane properties, and neurotransmitters. Physiol Rev 75:1-45.

Brockhaus J, Ballanyi K (1998) Synaptic inhibition in the isolated respiratory network of neonatal rats. Eur J Neurosci 10:3823-3839.

Butera RJ, Jr., Rinzel J, Smith JC (1999a) Models of respiratory rhythm generation in the pre-Botzinger complex. II. Populations Of coupled pacemaker neurons. J Neurophysiol 82:398-415.

Butera RJ, Jr., Rinzel J, Smith JC (1999b) Models of respiratory rhythm generation in the pre-Botzinger complex. I. Bursting pacemaker neurons. J Neurophysiol 82:382-397.

Charpak S, Mertz J, Beaurepaire E, Moreaux L, Delaney K (2001) Odor-evoked calcium signals in dendrites of rat mitral cells. Proc Natl Acad Sci U S A 98:1230-1234.

Cohen MI (1979) Neurogenesis of respiratory rhythm in the mammal. Physiol Rev 59:1105-1173.

Del Negro CA, Johnson SM, Butera RJ, Smith JC (2001) Models of respiratory rhythm generation in the pre-Botzinger complex. III. Experimental tests of model predictions. J Neurophysiol 86:59-74.

Del Negro CA, Koshiya N, Butera RJ, Jr., Smith JC (2002) Persistent sodium current, membrane properties and bursting behavior of pre-botzinger complex inspiratory neurons in vitro. J Neurophysiol 88:2242-2250.

Del Negro CA, Morgado-Valle C, Hayes JA, Mackay DD, Pace RW, Crowder EA, Feldman JL (2005) Sodium and calcium current-mediated pacemaker neurons and respiratory rhythm generation. J Neurosci 25:446-453.

Denk W, Svoboda K (1997) Photon upmanship: why multiphoton imaging is more than a gimmick. Neuron 18:351-357.

Duffin J (2004) Functional organization of respiratory neurones: a brief review of current questions and speculations. Exp Physiol 89:517-529.

Eilers J (2000) Fast confocal fluorescence imaging. In Imaging neurons: a laboratory manual. Cold Spring Harbor Laboratory Press

Elsen FP, Ramirez JM (2005) Postnatal development differentially affects voltage-activated calcium currents in respiratory rhythmic versus nonrhythmic neurons of the pre-Bötzinger complex. J Neurophysiol 94(2):1423-31.

Eugenin J, Nicholls JG, Cohen LB, Muller KJ (2006) Optical recording from respiratory pattern generator of fetal mouse brainstem reveals a distributed network. Neuroscience 137:1221-1227.

Fan GY, Fujisaki H, Miyawaki A, Tsay RK, Tsien RY, Ellisman MH (1999) Video-rate scanning two-photon excitation fluorescence microscopy and ratio imaging with cameleons. Biophys J 76:2412-2420.

Feldman JL, Smith JC (1989) Cellular mechanisms underlying modulation of breathing pattern in mammals. Ann N Y Acad Sci 563:114-130.

Feldman JL, Janczewski WA (2006a) The Last Word: Point:Counterpoint authors respond to commentaries on "the parafacial respiratory group (pFRG)/pre-Botzinger complex (preBotC) is the primary site of respiratory rhythm generation in the mammal". J Appl Physiol 101:689.

Feldman JL, Del Negro CA (2006) Looking for inspiration: new perspectives on respiratory rhythm. Nat Rev Neurosci 7:232-242.

Feldman JL, Janczewski WA (2006b) Point:Counterpoint: The parafacial respiratory group (pFRG)/pre-Botzinger complex (preBotC) is the primary site of respiratory rhythm generation in the mammal. Counterpoint: the preBotC is the primary site of respiratory rhythm generation in the mammal. J Appl Physiol 100:2096-2097; discussion 2097-2098, 2103-2098.

Feldman JL, Mitchell GS, Nattie EE (2003) Breathing: rhythmicity, plasticity, chemosensitivity. Annu Rev Neurosci 26:239-266.

Fisher JA, Marchenko VA, Yodh AG, Rogers RF (2006) Spatiotemporal activity patterns during respiratory rhythmogenesis in the rat ventrolateral medulla. J Neurophysiol 95:1982-1991.

Fleet A, Ellis-Davies G, Bolsover S (1998) Calcium buffering capacity of neuronal cell cytosol measured by flash photolysis of calcium buffer NP-EGTA. Biochem Biophys Res Commun 250:786-790.

Fredholm BB, Battig K, Holmen J, Nehlig A, Zvartau EE (1999) Actions of caffeine in the brain with special reference to factors that contribute to its widespread use. Pharmacol Rev 51:83-133.

Fung ML, St John WM (1995) The functional expression of a pontine pneumotaxic centre in neonatal rats. J Physiol 489 ( Pt 2):579-591.

Fung ML, St John WM (1998) Pontine cholinergic respiratory depression in neonatal and young rats. Life Sci 62:2249-2256.

Funk GD, Smith JC, Feldman JL (1993) Generation and transmission of respiratory oscillations in medullary slices: role of excitatory amino acids. J Neurophysiol 70:1497-1515.

Gray PA, Rekling JC, Bocchiaro CM, Feldman JL (1999) Modulation of respiratory frequency by peptidergic input to rhythmogenic neurons in the preBotzinger complex. Science 286:1566-1568.

Gray PA, Janczewski WA, Mellen N, McCrimmon DR, Feldman JL (2001) Normal breathing requires preBotzinger complex neurokinin-1 receptor-expressing neurons. Nat Neurosci 4:927-930.

Hall JD, Betarbet S, Jaramillo F (1997) Endogenous buffers limit the spread of free calcium in hair cells. Biophys J 73:1243-1252.

Hayes JA, Del Negro CA (2007) Neurokinin receptor-expressing pre-botzinger complex neurons in neonatal mice studied in vitro. J Neurophysiol 97:4215-4224.

Helmchen F, Svoboda K, Denk W, Tank DW (1999) In vivo dendritic calcium dynamics in deep-layer cortical pyramidal neurons. Nat Neurosci 2:989-996.

Hernandez-Cruz A, Sala F, Adams PR (1990) Subcellular calcium transients visualized by confocal microscopy in a voltage-clamped vertebrate neuron. Science 247:858-862.

Hwang JC, Chien CT, St John WM (1988) Characterization of respiratory-related activity of the facial nerve. Respir Physiol 73:175-187.

Janczewski WA, Feldman JL (2006) Distinct rhythm generators for inspiration and expiration in the juvenile rat. J Physiol 570:407-420.

Janczewski WA, Onimaru H, Homma I, Feldman JL (2002) Opioid-resistant respiratory pathway from the preinspiratory neurones to abdominal muscles: in vivo and in vitro study in the newborn rat. J Physiol 545:1017-1026.

Johnson SM, Koshiya N, Smith JC (2001) Isolation of the kernel for respiratory rhythm generation in a novel preparation: the pre-Botzinger complex "island". J Neurophysiol 85:1772-1776.

Kawai A, Okada Y, Muckenhoff K, Scheid P (1995) Theophylline and hypoxic ventilatory response in the rat isolated brainstem-spinal cord. Respir Physiol 100:25-32.

Koester HJ, Baur D, Uhl R, Hell SW (1999) Ca2+ fluorescence imaging with pico- and femtosecond two-photon excitation: signal and photodamage. Biophys J 77:2226-2236.

Koshiya N, Smith JC (1999) Neuronal pacemaker for breathing visualized in vitro. Nature 400:360-363.

Kuwana S, Tsunekawa N, Yanagawa Y, Okada Y, Kuribayashi J, Obata K (2006) Electrophysiological and morphological characteristics of GABAergic respiratory neurons in the mouse pre-Botzinger complex. Eur J Neurosci 23:667-674.

Ladewig T, Keller BU (2000) Simultaneous patch-clamp recording and calcium imaging in a rhythmically active neuronal network in the brainstem slice preparation from mouse. Eur J Physiol 440(2):322-32.

Lieske SP, Thoby-Brisson M, Telgkamp P, Ramirez JM (2000) Reconfiguration of the neural network controlling multiple breathing patterns: eupnea, sighs and gasps [see comment]. Nat Neurosci 3:600-607.

Lieske SP, Ramirez JM (2006a) Pattern-specific synaptic mechanisms in a multifunctional network. I. Effects of alterations in synapse strength. J Neurophysiol 95:1323-1333.

Lieske SP, Ramirez JM (2006b) Pattern-specific synaptic mechanisms in a multifunctional network. II. Intrinsic modulation by metabotropic glutamate receptors. J Neurophysiol 95:1334-1344.

Long S, Duffin J (1986) The neuronal determinants of respiratory rhythm. Prog Neurobiol 27:101-182.

McCrimmon DR, Zuperku EJ, Hayashi F, Dogas Z, Hinrichsen CF, Stuth EA, Tonkovic-Capin M, Krolo M, Hopp FA (1997) Modulation of the synaptic drive to respiratory premotor and motor neurons. Respir Physiol 110:161-176.

Mellen NM, Janczewski WA, Bocchiaro CM, Feldman JL (2003) Opioid-induced quantal slowing reveals dual networks for respiratory rhythm generation. Neuron 37:821-826.

Mironov SL, Richter DW (2001) Oscillations and hypoxic changes of mitochondrial variables in neurons of the brainstem respiratory centre of mice. J Physiol 15;533(Pt 1):227-36.

Mitchell GS, Johnson SM (2003) Neuroplasticity in respiratory motor control. J Appl Physiol 94:358-374.

Morgado C, Beltran-Parrazan L, Difranco M, Vergara JL, Feldman JL (2007) Ca2+ dynamics in active preBötzinger Complex (preBötC) inspiratory neurons. Online abstract. Society for Neuroscience, 2007.

Mulkey DK, Stornetta RL, Weston MC, Simmons JR, Parker A, Bayliss DA, Guyenet PG (2004) Respiratory control by ventral surface chemoreceptor neurons in rats. Nat Neurosci 7:1360-1369.

Oheim M, Beaurepaire E, Chaigneau E, Mertz J, Charpak S (2001) Two-photon microscopy in brain tissue: parameters influencing the imaging depth. J Neurosci Methods 111:29-37.

Okada Y, Chen Z, Yoshida H, Kuwana S, Jiang W, Maruiwa H (2001) Optical recording of the neuronal activity in the brainstem-spinal cord: application of a voltage-sensitive dye. Adv Exp Med Biol 499:113-118.

Onimaru H, Homma I (1987) Respiratory rhythm generator neurons in medulla of brainstem-spinal cord preparation from newborn rat. Brain Res 403:380-384.

Onimaru H, Homma I (2003) A novel functional neuron group for respiratory rhythm generation in the ventral medulla. J Neurosci 23:1478-1486.

Onimaru H, Homma I (2005) Optical imaging of respiratory neuron activity from the dorsal view of the lower brainstem. Clin Exp Pharmacol Physiol 32:297-301.

Onimaru H, Homma I (2006) Point:Counterpoint: The parafacial respiratory group (pFRG)/pre-Botzinger complex (preBotC) is the primary site of respiratory rhythm generation in the mammal. Point: the PFRG is the primary site of respiratory rhythm generation in the mammal. J Appl Physiol 100:2094-2095.

Onimaru H, Arata A, Homma I (1987) Localization of respiratory rhythm-generating neurons in the medulla of brainstem-spinal cord preparations from newborn rats. Neurosci Lett 78:151-155.

Onimaru H, Arata A, Homma I (1989) Firing properties of respiratory rhythm generating neurons in the absence of synaptic transmission in rat medulla in vitro. Exp Brain Res 76:530-536.

Onimaru H, Arata A, Homma I (1990) Inhibitory synaptic inputs to the respiratory rhythm generator in the medulla isolated from newborn rats. Pflugers Arch 417:425-432.

Onimaru H, Kanamaru A, Homma I (1996) Optical imaging of respiratory burst activity in newborn rat medullary block preparations. Neurosci Res 25:183-190.

Onimaru H, Kumagawa Y, Homma I (2006) Respiration-related rhythmic activity in the rostral medulla of newborn rats. J Neurophysiol 96:55-61.

Pagliardini S, Adachi T, Ren J, Funk GD, Greer JJ (2005) Fluorescent tagging of rhythmically active respiratory neurons within the pre-Botzinger complex of rat medullary slice preparations. J Neurosci 25:2591-2596.

Patterson GH, Piston DW (2000) Photobleaching in two-photon excitation microscopy. Biophys J 78:2159-2162.

Paton JF (1996) The ventral medullary respiratory network of the mature mouse studied in a working heart-brainstem preparation. J Physiol 493 ( Pt 3):819-831.

Pena F, Parkis MA, Tryba AK, Ramirez JM (2004) Differential contribution of pacemaker properties to the generation of respiratory rhythms during normoxia and hypoxia. Neuron 43:105-117.

Petran M, Hadravsky M, Benes J, Boyde A (1986) In vivo microscopy using the tandem scanning microscope. Ann N Y Acad Sci 483:440-447.

Potts JT, Paton JF (2006) Optical imaging of medullary ventral respiratory network during eupnea and gasping in situ. Eur J Neurosci 23:3025-3033.

Ptak K, Zummo GG, Alheid GF, Tkatch T, Surmeier DJ, McCrimmon DR (2005) Sodium currents in medullary neurons isolated from the pre-Botzinger complex region. J Neurosci 25:5159-5170.

Rajadhyaksha M, Gonzalez S, Zavislan JM, Anderson RR, Webb RH (1999) In vivo confocal scanning laser microscopy of human skin II: advances in instrumentation and comparison with histology. J Invest Dermatol 113:293-303.

Ramirez JM, Schwarzacher SW, Pierrefiche O, Olivera BM, Richter DW (1998) Selective lesioning of the cat pre-Botzinger complex in vivo eliminates breathing but not gasping. J Physiol 507 ( Pt 3):895-907.

Rekling JC, Champagnat J, Denavit-Saubie M (1996) Electroresponsive properties and membrane potential trajectories of three types of inspiratory neurons in the newborn mouse brain stem in vitro. J Neurophysiol 75:795-810.

Richter DW (1982) Generation and maintenance of the respiratory rhythm. J Exp Biol 100:93-107.

Richter DW, Spyer KM (2001) Studying rhythmogenesis of breathing: comparison of in vivo and in vitro models. Trends Neurosci 24:464-472.

Richter DW, Ballanyi K, Schwarzacher S (1992) Mechanisms of respiratory rhythm generation. Curr Opin Neurobiol 2:788-793.

Ruangkittisakul A, Secchia L, Bornes TD, Palathinkal DM, Ballanyi K (2007a) Dependence on extracellular Ca2+/K+ antagonism of inspiratory centre rhythms in slices and en bloc preparations of newborn rat brainstem. J Physiol 584:489-508.

Ruangkittisakul A, Schwarzacher SW, Secchia L, Ma Y, Bobocea N, Poon BY, Funk GD, Ballanyi K (2007b) Eupnea and sighs: the two sides of the reconfiguring inspiratory center. In preparation.

Ruangkittisakul A, Schwarzacher SW, Secchia L, Poon BY, Ma Y, Funk GD, Ballanyi K (2006) High sensitivity to neuromodulator-activated signaling pathways at physiological [K+] of confocally imaged respiratory center neurons in on-line-calibrated newborn rat brainstem slices. J Neurosci 26:11870-11880.

Shao XM, Feldman JL (1997) Respiratory rhythm generation and synaptic inhibition of expiratory neurons in pre-Botzinger complex: differential roles of glycinergic and GABAergic neural transmission. J Neurophysiol 77:1853-1860.

Smith JC, Greer JJ, Liu GS, Feldman JL (1990) Neural mechanisms generating respiratory pattern in mammalian brain stem-spinal cord in vitro. I. Spatiotemporal patterns of motor and medullary neuron activity. J Neurophysiol 64:1149-1169.

Smith JC, Ellenberger HH, Ballanyi K, Richter DW, Feldman JL (1991) Pre-Botzinger complex: a brainstem region that may generate respiratory rhythm in mammals. Science 254:726-729.

Smith JC, Butera RJ, Koshiya N, Del Negro C, Wilson CG, Johnson SM (2000) Respiratory rhythm generation in neonatal and adult mammals: the hybrid pacemaker-network model. Respir Physiol 122:131-147.

Solomon IC, Edelman NH, Neubauer JA (1999) Patterns of phrenic motor output evoked by chemical stimulation of neurons located in the pre-Botzinger complex in vivo. J Neurophysiol 81:1150-1161.

Somjen GG (2002) Ion regulation in the brain: implications for pathophysiology. Neuroscientist 8:254-267.

St-John WM, Paton JF (2004) Role of pontile mechanisms in the neurogenesis of eupnea. Respir Physiol Neurobiol 143:321-332.

St -John WM, Paton JF (2003) Defining eupnea. Respir Physiol Neurobiol 139:97-103.

Stosiek C, Garaschuk O, Holthoff K, Konnerth A (2003) In vivo two-photon calcium imaging of neuronal networks. Proc Natl Acad Sci USA 100:7319 –7324.

Strohl KP (1985) Respiratory activation of the facial nerve and alar muscles in anaesthetized dogs. J Physiol 363:351-362.

Svoboda K, Denk W, Kleinfeld D, Tank DW (1997) In vivo dendritic calcium dynamics in neocortical pyramidal neurons. Nature 385:161-165.

Suzue T (1984) Respiratory rhythm generation in the in vitro brain stem-spinal cord preparation of the neonatal rat. J Physiol 354:173-83.

Telgkamp P, Cao YQ, Basbaum AI, Ramirez JM (2002) Long-term deprivation of substance P in PPT-A mutant mice alters the anoxic response of the isolated respiratory network. J Neurophysiol 88:206-213.

Thoby-Brisson M, Trinh JB, Champagnat J, Fortin G (2005) Emergence of the pre-Botzinger respiratory rhythm generator in the mouse embryo. J Neurosci 25:4307-4318.

Tokumasu M, Nakazono Y, Ide H, Akagawa K, Onimaru H (2001) Optical recording of spontaneous respiratory neuron activity in the rat brain stem. Jpn J Physiol 51:613-619.

Tryba AK, Pena F, Ramirez JM (2006) Gasping activity in vitro: a rhythm dependent on 5-HT2A receptors. J Neurosci 26:2623-2634.

Tsien RY, Bacskai BJ (1995) Video-rate confocal microscopy. In Handbook of biological confocal microscopy, 2nd edition (ed. Pawley JB). Plenum Press, NY

Yuste R, Konnerth A, Masters BR (2006) Imaging in neuroscience and development, a laboratory manual. J Biomed Opt 11:19902.

Winter SM, Hirrlinger J, Kirchhoff F, Hulsmann S (2007) Transgenic expression of fluorescent proteins in respiratory neurons. Respir Physiol Neurobiol 159:108-114.